A near-infrared interferometric survey of debris-disk stars. VII. The hot-to-warm dust connection

O. Absil, L. Marion, S. Ertel, D. Defrère, G. M. Kennedy, A. Romagnolo, J. -B. Le Bouquin, V. Christiaens, J. Milli, A. Bonsor, et al.

A&A 651, A45 (2021)
https://doi.org/10.1051/0004-6361/202140561

Astronomy & Astrophysics

A near-infrared interferometric survey of debris-disk stars

VII. The hot-to-warm dust connection★

O. Absil[1,★★], L. Marion[1], S. Ertel[2,3], D. Defrère[4], G. M. Kennedy[5], A. Romagnolo[6], J.-B. Le Bouquin[7], V. Christiaens[8], J. Milli[7], A. Bonsor[9], J. Olofsson[10,11], K. Y. L. Su[3], and J.-C. Augereau[7]

[1] STAR Institute, Université de Liège, 19c Allée du Six Août, 4000 Liège, Belgium
e-mail: olivier.absil@uliege.be
[2] Large Binocular Telescope Observatory, 933 North Cherry Avenue, Tucson, AZ 85721, USA
[3] Steward Observatory, Department of Astronomy, University of Arizona, 993 N. Cherry Ave, Tucson, AZ, 85721, USA
[4] Institute of Astronomy, KU Leuven, Celestijnlaan 200D, 3001 Leuven, Belgium
[5] Department of Physics, University of Warwick, Gibbet Hill Road, Coventry, CV4 7AL, UK
[6] Nicolaus Copernicus Astronomical Center, Polish Academy of Sciences, Bartycka 18, 00-716, Warsaw, Poland
[7] Univ. Grenoble Alpes, CNRS, IPAG, 38000 Grenoble, France
[8] School of Physics and Astronomy, Monash University, Clayton, Vic 3800, Australia
[9] Institute of Astronomy, University of Cambridge, Madingley Road, Cambridge CB3 0HA, UK
[10] Instituto de Física y Astronomía, Facultad de Ciencias, Universidad de Valparaíso, Av. Gran Bretaña 1111, Playa Ancha, Valparaíso, Chile
[11] Núcleo Milenio Formación Planetaria - NPF, Universidad de Valparaíso, Av. Gran Bretaña 1111, Valparaíso, Chile

Received 15 February 2021 / Accepted 21 April 2021

ABSTRACT

Context. Hot exozodiacal dust has been shown to be present in the innermost regions of an increasing number of main sequence stars over the past 15 yr. However, the origin of hot exozodiacal dust and its connection with outer dust reservoirs remains unclear.
Aims. We aim to explore the possible connection between hot exozodiacal dust and warm dust reservoirs (≥100 K) in asteroid belts.
Methods. We use precision near-infrared interferometry with VLTI/PIONIER to search for resolved emission at H-band around a selected sample of 62 nearby stars that show possible signs of warm dust populations.
Results. Our observations reveal the presence of resolved near-infrared emission around 17 out of 52 stars with sufficient data quality. For four of these, the emission is shown to be due to a previously unknown stellar companion. The 13 other H-band excesses are thought to originate from the thermal emission of hot dust grains, close to their sublimation temperature. Taking into account earlier PIONIER observations, where some stars with warm dust were also observed, and after re-evaluating the warm dust content of all our PIONIER targets through spectral energy distribution modeling, we find a detection rate of $17.1^{+8.1}_{-4.6}$% for H-band excess around main sequence stars hosting warm dust belts, which is statistically compatible with the occurrence rate of $14.6^{+4.3}_{-2.8}$% found around stars showing no signs of warm dust. After correcting for the sensitivity loss due to partly unresolved hot disks, under the assumption that they are arranged in a thin ring around their sublimation radius, we find tentative evidence at the 3σ level that H-band excesses around stars with outer dust reservoirs (warm or cold) could be statistically larger than H-band excesses around stars with no detectable outer dust.
Conclusions. Our observations do not suggest a direct connection between warm and hot dust populations at the sensitivity level of the considered instruments, although they bring to light a possible correlation between the level of H-band excess and the presence of outer dust reservoirs in general.

Key words. circumstellar matter – binaries close – techniques: interferometric

1. Introduction

Studying the formation and evolution of potentially habitable Earth-like planets requires a good knowledge of the environment close to the habitable zone, and thus of the *exozodiacal* dust residing in this region (similar to our zodiacal dust). The presence of exozodiacal dust around other stars may represent a major obstacle for future terrestrial planet-finding missions (Defrère et al. 2010, 2012; Roberge et al. 2012; Stark et al. 2014a). Indeed, exozodiacal dust disks ("exozodis") not only add a significant amount of photon noise to the observations, but may also result in confusion, where the structures of the exozodis mimic the expected signal of an Earth-like planet as seen by future coronagraphic or interferometric space-based observatories. Usually, when referring to exozodiacal dust, one considers primarily the dust in the habitable zone (e.g., Defrère et al. 2010; Roberge et al. 2012; Stark & Kuchner 2008). However, in our Solar System, zodiacal dust is much more extended than the habitable zone, and actually shows an increasing density down to the F-corona, with a possible dust-free zone within 0.1–0.2 au of the Sun (e.g., Dikarev & Schwarz 2015; Howard et al. 2019). Likewise, it is expected that exozodiacal dust can extend over a broad range of

★ Based on observations made with ESO Telescopes at the La Silla Paranal Observatory under program IDs 093.C-0712 and 094.C-0325.
★★ F.R.S.-FNRS Research Associate.

separations from its host star, covering a zone much larger than just the habitable one.

The capability of near-infrared interferometry to probe the presence of hot dust in the innermost regions around nearby stars was first demonstrated by Ciardi et al. (2001) and Absil et al. (2006). The study of Absil et al. (2006) was then followed by a series of papers, which have extended the search to about 150 nearby stars, mostly using the CHARA/FLUOR and VLTI/PIONIER instruments (Absil et al. 2006, 2008, 2013; di Folco et al. 2007; Ertel et al. 2014; Nuñez et al. 2017). These studies have shown that near-infrared excesses can be resolved around about 10% to 30% of nearby main sequence stars depending on the observing wavelength. Ertel et al. (2016) also demonstrated the repeatability of the detections, showing that near-infrared excesses are not spurious or caused by poorly understood instrumental or astrophysical errors. Our current understanding is that near-infrared excesses around main sequence stars are related to the thermal emission from hot dust grains close to their sublimation temperature (~1500 K for silicate dust grains). The contribution of scattered light cannot be excluded in some cases (di Folco et al. 2007; Mennesson et al. 2011; Defrère et al. 2012; Ertel et al. 2014), although recent polarimetric, interferometric, and theoretical studies argue against scattered light as a prominent contributor to the detected excesses (Kennedy & Piette 2015; Kennedy et al. 2015; Marshall et al. 2016; Kirchschlager et al. 2017, 2020). These previous studies highlighted a tentative correlation between spectral type and near-infrared excess detection rate, but could not formally identify any correlation between the presence of hot dust and of cold, distant dust reservoirs detected by far-infrared and submillimeter photometry. The factors influencing the presence of hot exozodiacal dust around nearby main sequence stars are therefore still unclear, which calls for more observational constraints.

Here, we study the possible correlation of the hot dust phenomenon with the presence of warm asteroid belts around nearby main sequence stars. We define warm dust as dust producing a detectable excess in the mid-infrared but not in near-infrared (typical temperatures in the range 100–500 K), while hot dust is defined as dust producing an excess in the near-infrared (see Fig. 1). Our main goal is to determine whether or not the presence of hot exozodiacal dust is directly related to the presence of a large reservoir of planetesimals in an asteroid belt, in an attempt to improve our understanding of the origin, architecture, and evolution of bright exozodiacal dust disks, as well as of the factors influencing their detection rate. To this aim, we build a sample of stars known to have a mid-infrared excess attributed to debris disks based on infrared space missions such as *Spitzer* and WISE (Sect. 2). After detailing the PIONIER observations and data reduction in Sect. 3, we present in Sect. 4 the search for unknown companions in this sample – a necessary step to remove possible contamination in our sample. In Sect. 5, we present the search for hot exozodis in this sample, detailing the search method and the results. Finally, in Sect. 6, we discuss the connection between hot and warm dust. We also challenge the standard hypothesis of fully resolved exozodis in interferometric observations, and explore the consequences of partly resolved disks on the measured detection rates.

2. Stellar sample

Searching for correlations between hot and warm dust populations first requires a sufficiently large sample of nearby stars hosting warm dust. Three main space-based missions have been used to search for warm dust around nearby stars: *Spitzer*, AKARI, and WISE. We searched the literature for warm excesses around nearby stars, focusing mostly on these three missions (Carpenter et al. 2009; Chen et al. 2006, 2014; Hillenbrand et al. 2008; Ishihara et al. 2010; Morales et al. 2012; Ballering et al. 2013; Fujiwara et al. 2013; Vican & Schneider 2014; Patel et al. 2014). To identify warm dust, these missions rely on spectrophotometric observations at wavelengths shorter than 25 µm. However, showing a mid-infrared excess is not a sufficient condition to infer the presence of warm dust, as excesses in this wavelength range can sometimes correspond to the short-wavelength end of a bright but cold circumstellar emission. We originally built our sample based on the dust temperature estimated in the literature using a threshold of 130 K[1] as a criterion to distinguish warm from cold populations, following Ballering et al. (2013). In several cases, the warm excesses could only be detected at a single wavelength, making an accurate temperature determination impossible. In these cases, the authors generally quote the highest possible temperature compatible with their data set. Lacking more precise information, we decided to use these upper limits as a criterion to select stars with possible warm dust populations, where applicable. While our previous near-infrared interferometric surveys were targeting stars brighter than $H = 5$, to build a sufficiently large sample here, we include stars up to $H = 7$, which remains comfortably within the magnitude limit of VLTI/PIONIER. Stars with visual companions within the interferometric field of view of PIONIER on the VLTI Auxiliary Telescopes (~400 mas full width at half maximum in H band) are not appropriate for detecting weak, extended circumstellar emission. Even light from companions outside the field of view may enter the optical path when there is bad seeing. Thus, as in Ertel et al. (2014), all known binary systems with angular

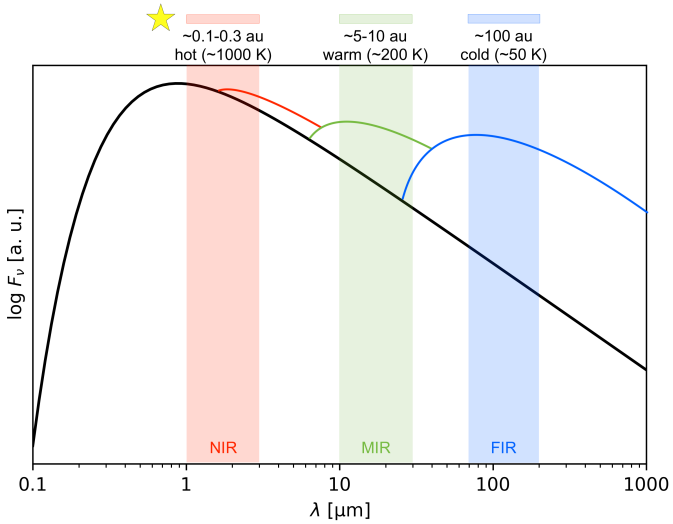

Fig. 1. Illustration of the typical orbital distances and temperatures for the hot, warm, and cold dust belts considered in this work, and of the corresponding wavelength ranges in terms of spectral energy distribution. Adapted from Kirchschlager et al. (2017).

[1] This temperature threshold of 130 K was only used to select our target stars based on the available literature in 2013. We discuss below that a temperature of 100 K was finally chosen to distinguish between warm and cold dust populations. A significant fraction of the selected targets actually turned out not to show the presence of any warm dust after re-evaluation of their mid- to far-infrared excess, as described in Sect. 2.1.

separation <5″ are removed from our sample. We identified a total of 62 stars meeting our criteria, which had not been observed yet with precision near-infrared interferometry. The main properties of these 62 targets to be observed with PIONIER are summarized in Table B.1. We collected PIONIER data of sufficient quality for only 52 of them, as described in Sect. 3. Furthermore, 4 of these 52 stars turned out to be binaries based on our PIONIER observations (see Sect. 4). These binary stars are not amenable to a search for exozodiacal dust, and are therefore removed from our sample, meaning that we are left with 48 new stars to study the correlation between warm and hot dust.

To assess a possible correlation between the presence of hot and warm dust, we also need to build a control sample. Our control sample is based on the VLTI/PIONIER survey for hot exozodiacal dust carried out by Ertel et al. (2014). The reader is referred to that paper for a detailed description of the stellar parameters of this sample. Among the 85 single and non-evolved stars included in that sample, given the literature, we expected a large majority of them to not host any warm dust population, based on the absence of mid-infrared excesses. However, we note that the warm versus cold dust classification derived from the dust temperatures described in the literature is inconsistent, because of the various assumptions made in the publications of these mid-infrared surveys. We therefore decided to re-assess the presence of warm dust around the 133 stars included in both the Ertel et al. (2014) sample (85 stars) and our new sample (48 stars).

2.1. Reassessing the presence of warm and cold dust

In order to reassess the presence of warm and/or cold dust around our combined sample of 133 stars, we collected photometry at all available optical, mid-, and far-infrared wavelengths for all targets. In most cases, these are available in literature catalogs, for example for optical *UVB* and *ubvy* data (Mermilliod 1987; Paunzen 2015), and 2MASS and WISE infrared data (Cutri et al. 2003; Wright et al. 2010). However, far-infrared photometry for our targets is either unpublished or spread across many different analyses. To maximize consistency, *Spitzer*/MIPS photometry at 24 and 70 μm uses our own updated PSF fitting for all targets, as described in Sierchio et al. (2014) and Yelverton et al. (2019), except four bright targets, which use 70 μm photometry from Chen et al. (2014). *Herschel*/PACS photometry at 70, 100, and 160 μm, and SPIRE photometry at 250, 350, and 500 μm also uses our PSF fitting, as described in Sibthorpe et al. (2018). We also use *Spitzer*/IRS spectra from the CASSIS archive (Lebouteiller et al. 2011), where available.

The data for each star are initially fit with a star + disk model using the `sdf` code, as described by Yelverton et al. (2019). The star is a BT-Settl photosphere model (Allard et al. 2012) and the disk is a modified blackbody (a Planck function that is multiplied by $\lambda_0^{-\beta}$ at wavelengths longer than λ_0), and the fitting is done using the `multinest` code (Feroz et al. 2009). The fitting serves two purposes, firstly to provide an estimate of the stellar flux at all wavelengths to allow the presence of any infrared excess to be quantified, and secondly to estimate the temperature and luminosity of any disk if the excess is deemed significant as described below (if no excess is present the disk component has negligible flux by definition, and is not used). In some cases the single-component disk provides a poor fit to the infrared excess, in which case a second disk component is added. Whether or not a second component is needed is somewhat subjective, because the true dust spectrum is unknown and might mimic a two-component disk (Kennedy & Wyatt 2014). Our assessment primarily considers whether two disk components are needed to fit all photometry and the IRS spectrum, but also considers whether the dust temperatures of a two-component fit are sufficiently different (Kennedy & Wyatt 2014).

To assess whether or not infrared excesses are significant, we use the empirical method used by many previous studies (e.g., Su et al. 2006; Ertel et al. 2014; Yelverton et al. 2020), which we also use below for the PIONIER observations. Essentially, we assume that most stars do not have a significant excess, and therefore that the distribution of excess significance in a given band i,

$$\chi_i = \frac{F_{\rm obs} - F_\star}{\sqrt{\sigma_{\rm obs}^2 + \sigma_\star^2}}, \quad (1)$$

should be approximately Gaussian with zero mean and unity standard deviation. Any positive outliers with $\chi_i > 3$ would therefore be considered as having a significant excess. If the standard deviation is greater or smaller than unity, as is commonly the case, the uncertainties for that band are considered to be under- or overestimated, respectively, and the threshold for an excess adjusted accordingly. For example, Yelverton et al. (2020) found the standard deviation for PACS 100 μm to be 1.68, and therefore set the threshold for an excess to be 3×1.68. In general, the IRS spectra were used as important input for deriving disk temperatures, but in a few cases (HD 40307, HD 90874, HD 91324) were also used to confirm an excess that was not significant photometrically (because of low signal-to-noise ratio (S/N) and/or poor wavelength coverage).

We decided to classify as dusty any stellar system whose excess significance was beyond four standard deviations from the average ($\chi > \mu + 4\sigma$) in at least one band. In order to keep an average excess significance around zero in our noise distributions, the Gaussian fitting of the noise distribution was done without any star with $\chi > 3$. In the case of PACS70, there were not enough data points to fit an appropriate Gaussian distribution. We therefore explored the possibility to use the noise distributions from Yelverton et al. (2019) for that filter. In Fig. 2, we compare our Gaussian fit to the PACS100 significance with the ones obtained by Yelverton et al. (2019) for their PACS70 and PACS100 data sets. The difference in terms of outliers was found to be marginal: only the excesses of two additional stars (namely HD 7570 for PACS100, and HD 174474 for PACS70) were significant with the use of Yelverton et al. (2019) parameters but not with ours. We therefore decided to adopt the Gaussian noise distributions fitted by Yelverton et al. (2019) for our PACS70 and PACS100 data sets. The χ histograms for the remaining four WISE and MIPS filters are plotted in Fig. 3 with their respective noise distributions.

Among the 133 stars in our combined sample, 68 show the presence of circumstellar dust in their mid- to far-infrared SED based on our analysis (see Appendix A for an illustration of all 133 SEDs). In order to separate these 68 stars into two categories (warm and cold dust), we set an arbitrary limit of 100 K to distinguish between the two populations. The new warm or cold dust classification for these 68 stars is given in Table B.2. We note that two stars (HD 36187 and HD 89886) do not have sufficient mid- to far-infrared data to conclude on the temperature of the detected excess. These two stars are therefore removed from our warm and cold dust samples, leaving us with a total of 131 stars, among which 66 show the presence of circumstellar dust.

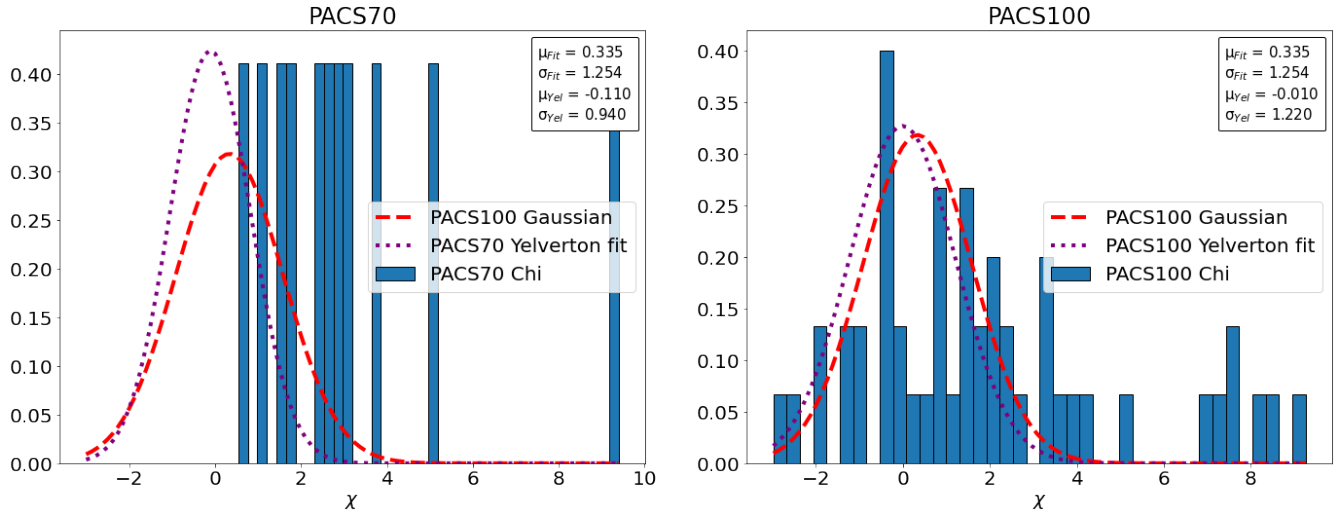

Fig. 2. Histograms of excess significance for PACS70 (*left*) and PACS100 (*right*) measurements. The purple dotted curve shows the noise distribution derived by Yelverton et al. (2019) for their PACS70 (*left*) and PACS100 (*right*) data sets, while the red dashed curve shows the same noise distribution derived from our PACS100 data set – our PACS70 data set was not large enough to robustly fit the noise distribution. The values noted as $\mu_{\rm Fit}$ and $\sigma_{\rm Fit}$ are respectively the mean and standard deviation of the significance in our PACS100 distribution, while $\mu_{\rm Yel}$ and $\sigma_{\rm Yel}$ are the ones from Yelverton et al. (2019).

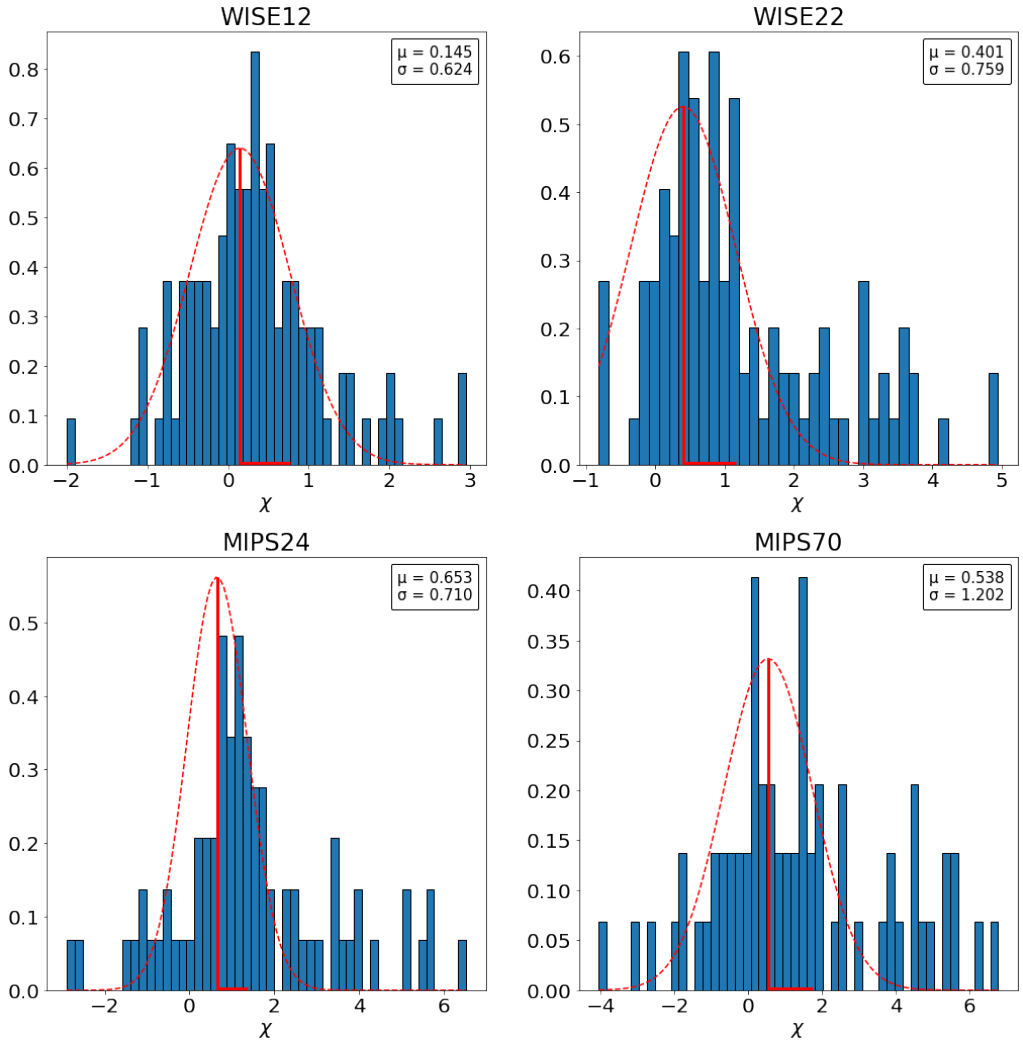

Fig. 3. Histograms of excess significance for WISE12 (*top left*), WISE22 (*top right*), MIPS24 (*bottom left*), and MIPS70 (*bottom right*), together with their best-fit Gaussian noise distribution (red dashed curve). The mean (μ) and standard deviation (σ) of the noise distributions are also plotted respectively as red vertical and horizontal lines. Significance values lower than −4 and higher than 8 are not displayed for the sake of clarity.

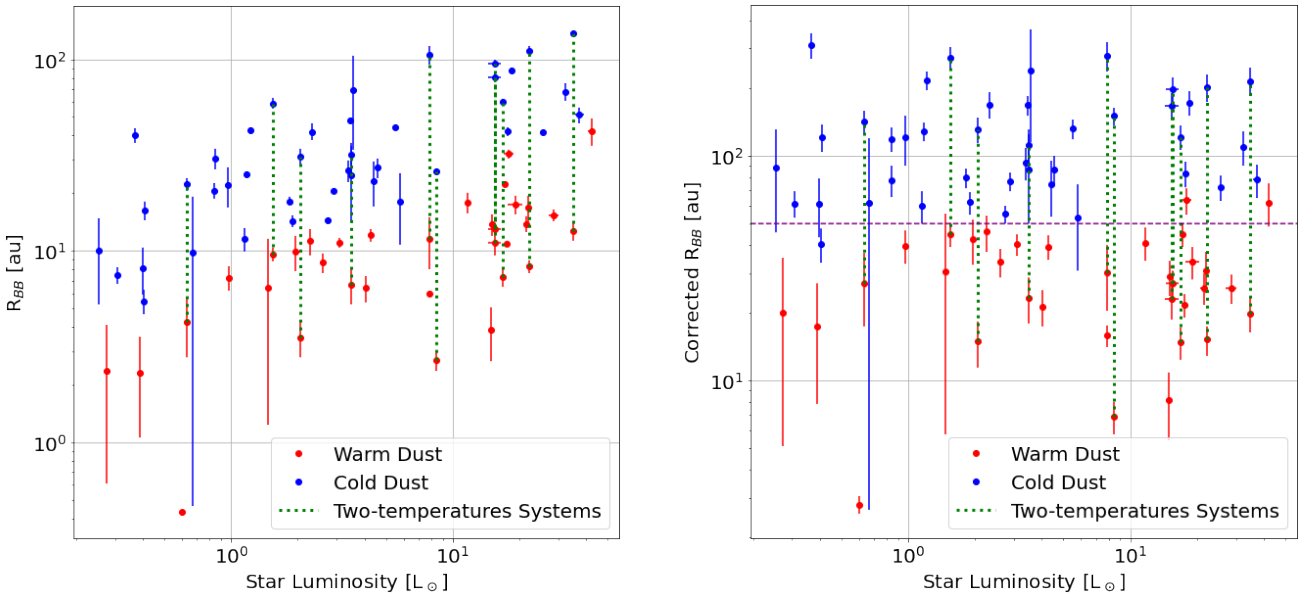

Fig. 4. *Left panel*: equivalent blackbody radius of the dust disks around the 66 stars in our combined sample showing a significant mid- to far-infrared excess, for which a dust temperature could be derived. Disks classified as warm (>100 K) and as cold (<100 K) are colored red and blue respectively. *Right panel*: same as left, but for the corrected blackbody radius, using the 50% astrosilicate + 50% ice composition of Pawellek & Krivov (2015). A purple dashed line at 50 au shows a rough separation between warm and cold dust populations. The vertical green dotted lines link the warm and the cold dusts that were found in the same stellar system.

2.2. Statistics of our combined sample

Based on our SED modeling, our final sample of 131 stars contains a total of 35 stars that show the presence of warm dust populations (> 100 K), among which 11 also show the presence of a cold dust reservoir (<100 K). Another 31 stars show the presence of cold dust only, while 65 stars show no sign of circumstellar dust, at a sensitivity level that depends on the stellar brightness and spectral type, and on the quality of the mid- to far-infrared observations available for each star. For the 66 stars that show the presence of circumstellar dust, Fig. 4 shows the equivalent blackbody radius of the dust disk, as well as the corrected blackbody radius following Pawellek & Krivov (2015), using a 50% astrosilicate +50% ice composition. The correction takes into account the blow-out of the smallest dust grains, and is meant to provide a more representative estimate of the true radius of a spatially unresolved dust disk. The right-hand plot in Fig. 4 shows that our 100 K criterion corresponds more or less to a 50 au limit in terms of corrected blackbody radius between the warm and cold dust disks, although some A-type stars show warm dust up to about 60 au, while late-type stars show cold dust down to about 40 au. This relatively good agreement between our temperature classification and a classification based on the corrected blackbody distance to the host star provides an independent justification to our classification strategy. While a 50 au limit between warm and cold dust populations may seem large, it ensures that the two populations are balanced in size, and we argue in Sect. 6.1 that choosing a higher temperature threshold would not change the conclusions of our study.

While the dusty and nondusty samples are relatively equally spread between A-type, F-type, and G/K-type stars, with 33% ± 8% of stars in each of the three spectral type categories, it must be noted that the warm dust sample is largely biased towards A-type stars (with 18 A-type stars out 35), while the cold dust sample is biased towards G/K-type stars (14 G/K-type stars out of 31). This imbalance likely arises because disks tend to be warmer around earlier type stars (e.g., Kennedy & Wyatt 2014). This could also be partly due to the fact that warm dust appears up to larger orbital distances around A-type stars, even after taking into account the blackbody correction of Pawellek & Krivov (2015).

Our target stars mostly consist of old, main sequence field stars, generally not younger than a few hundred million years. A handful of stars in our sample are somewhat younger: HD 141943 (field star, 30 Myr, Chen et al. 2014); HD 203, HD 39060, HD 172555, HD 181327, and HD 191089 (part of the β Pic moving group, 21 Myr, Binks & Jeffries 2014); HD 192758 (part of IC 2391, 40 Myr, Wahhaj et al. 2013); HD 109573 (part of the TW Hya association, 10 Myr, Mittal et al. 2015); HD 106906 (part of the Lower Centaurus Crux association, 15 Myr, Pecaut & Mamajek 2016); and HD 188228 (part of the Argus association, 38 Myr, Booth et al. 2013). We note that the average stellar age of the warm dust sample (0.83 Gyr) is significantly lower than for the control sample (2.7 Gyr), which is not unexpected as the presence of warm dust is known to be correlated with the system age (e.g., Su et al. 2006; Vican & Schneider 2014). Any correlation between hot and warm dust will therefore also be tested for a possible age bias, although previous studies (e.g., Absil et al. 2013; Ertel et al. 2014) do not suggest a significant age dependence in the hot exozodi phenomenon.

3. Observations and data reduction

Observations were carried out with VLTI/PIONIER (Le Bouquin et al. 2011) at H band in April, August, and December 2014, each run consisting of three consecutive observing nights. An observing log of all nights can be found in Table 1. We used the four 1.8-m Auxiliary Telescopes (ATs) to obtain six visibility measurements simultaneously. We used an array configuration (D0-H0-G1-I1) with baselines ranging between 41 m and 82 m for all observing runs. This configuration is larger than the one used for the Ertel et al. (2014) survey, because the stars in the present sample are more distant on average and therefore require

Table 1. Summary of the new VLTI/PIONIER observations.

Run	Night	# stars	Seeing (″)	τ_0 (ms)	Notes
093.C-0712(A)	07-04-2014	7	1.6 (0.8–2.5)	1.4 (1.1–1.7)	Strong seeing at the end of the night
093.C-0712(A)	08-04-2014	9	1.7 (0.6–2.9)	2.2 (0.8–3.7)	Strong seeing in the middle of the night
093.C-0712(A)	09-04-2014	9	1.3 (0.6–2.0)	2.5 (1.3–3.8)	Some clouds
093.C-0712(B)	30-08-2014	8	1.2 (0.6–1.9)	1.7 (1.1–2.3)	Good conditions
093.C-0712(B)	31-08-2014	9	1.2 (0.6–1.9)	2.1 (1.0–3.2)	Some clouds
093.C-0712(B)	01-09-2014	4	1.1 (0.7–1.6)	3.2 (1.9–4.5)	Thin clouds, dome closed for a part of the night
094.C-0325(A)	22-12-2014	7	1.0 (0.5–1.5)	2.3 (1.4–3.2)	Good conditions
094.C-0325(A)	23-12-2014	11	1.4 (0.5–2.4)	2.3 (1.1–3.6)	Strong seeing at the beginning of the night
094.C-0325(A)	24-12-2014	8	1.5 (0.4–2.5)	3.1 (0.9–5.3)	Strong seeing at the beginning of the night

a higher angular resolution to resolve their sublimation radius (see Sect. 6.3 for more details). After the August run, the detector of PIONIER was changed, which implied a change in the read-out mode. The read-out mode was set to FOWLER with SMALL dispersion (three spectral channels) for the observations of April and August 2014, and to HIGH SENS with a GRISM dispersion (six spectral channels) for the observations of December 2014. Four calibrator stars were selected from Mérand et al. (2005) for each science target, typically within 10° on sky to minimize the effects of pupil rotation or instrumental polarization (see Le Bouquin et al. 2012). Additional selection criteria were an H-band magnitude similar to the science target, and a small angular diameter. Most of the targets were observed in a CAL1-SCI-CAL2-SCI-CAL3-SCI-CAL4 sequence, where two nonconsecutive calibrators can be the same.

Out of the 62 stars in our observing list, a total of 10 stars had to be removed from our final sample for various reasons. Four could not be appropriately observed: HD 141378 and HD 43879 because of incomplete observing sequences (not enough data), HD 59967 because of inappropriate calibrators, and HD 93453 because two out of the three SCI observations were obtained during a burst of bad seeing (>2″). The other six stars were removed after the data reduction and calibration procedure, as detailed below. The data reduction consists of the conversion of raw observations into calibrated interferometric observables. We use the exact same method as in Ertel et al. (2014). The first step of the calibration is to calibrate the instrumental visibility within the CAL-SCI-...-CAL sequence. To do so, we calibrate each SCI individually by pairing it with either the preceding or the following CAL. During this process, we also make sure we discard all calibrators with low S/N or with a clear closure phase signal (see Ertel et al. 2014, for details). After calibration, six stars had to be rejected from our sample (HD 4247, HD 10008, HD 31392, HD 142139, HD 178606, and HD 184932) because of large discontinuities in the interferometric transfer function[2] caused by poor seeing conditions, low coherence time, or clouds. The actual number of new stars added through this observing program therefore amounts to 52.

The last step in the data analysis procedure is to assess the systematic polarization effects of PIONIER. This part is automatically corrected by a dedicated option in the standard PIONIER pipeline (`pndrs`, Le Bouquin et al. 2011) used for the reduction. A detailed explanation of the polarization effects can be found in Ertel et al. (2014).

[2] The interferometric transfer function monitors the instrumental visibility, or instrumental closure phase, as a function of time.

4. Searching for companions

Before searching for hot exozodiacal disks based on our interferometric observations, we first need to identify possible unknown (sub)stellar companions that could also produce an infrared excess. This ensures that all our target stars are single.

4.1. Principle of the search

Following the same lines as in Absil et al. (2011) and Marion et al. (2014), we use the full information delivered by PIONIER (squared visibilities, V^2, and closure phases, CP) to systematically search for companions around all the stars. By doing so, we are able to distinguish whether the small near-infrared excess detected around some of the target stars is due to an extended, mostly symmetric source, or to a point-like companion. The method used to detect companions is fully described in Marion et al. (2014). Here, we provide a brief summary.

First, we define the search region, taking into account three main factors. The first factor is the Gaussian profile of the single-mode fiber used in PIONIER ($FWHM \approx 400$ mas). The second one is the finite scan length of the optical path delay. With the medium configuration used here and for a typical scan length of 100 μm, the maximum separation that can be probed is $\Delta\theta_{\max} \simeq 200$ mas, although we recognize that companions with separations larger than 70 mas may not be simultaneously visible on all baselines. The third factor to take into account is the sufficient sampling of the closure phase signal as a function of wavelength, which depends on the baseline and on the spectral resolution. Following Absil et al. (2011), the well-sampled field of view is about 50 mas in radius. Taking all of this into account, we consider a search region of 50 mas in radius in this study. However, we note that our search is actually sensitive to companions out to about 200 mas, with point-like sources between 50 and 200 mas creating aliasing within our 50 mas search region. As explained in Sect. 2, companions beyond 200 mas may bias our observations, but we expect that such companions (with contrasts of 1% or more) would have already been identified in the literature.

To detect the presence of a companion, we use the closure phases and the squared visibilities in a combined way. As in Marion et al. (2014), we build a binary model considering the primary star at the center of the search region with an off-axis companion of various contrast c at each point (x, y) of the search region. In the present case, we can safely assume that both the primary and the secondary stars are unresolved, because all of our targets have an angular diameter $\lesssim$0.5 mas. We then compute the V^2 and CP for each model and derive a combined goodness of fit that we normalize and collapse along the contrast axis to keep

Table 2. Summary of the stars showing a significance level higher than 5σ based on the analysis of the combined χ^2 (CP+V^2).

Name	Significance			Nature	Point-like source		
					Separation	PA	Contrast
	(CP+V^2)	(CP)	(V^2)		(mas)	(deg)	(%)
HD 203	5.4	3.7	7.3	disk	–	–	–
HD 31203	14.5	20.2	25.6	point-like	64.6 ± 1.3	-50.2 ± 0.4	4.3 ± 0.6
HD 36187	9.3	2.2	23.4	disk	–	–	–
HD 61005	6.7	2.5	7.7	disk	–	–	–
HD 76143	6.4	5.3	4.9	disk	–	–	–
HD 80133	4642.7	318.5	14 616.4	point-like	6.0 ± 0.2	13.2 ± 0.7	85.2 ± 2.6
HD 106906	145.0	12.0	509.1	point-like	1.4 ± 0.1	95.2 ± 5.1	95.0 ± 7.4
HD 175073	64.7	59.6	391.3	point-like	31.2 ± 0.6	-84.7 ± 0.4	13.0 ± 0.9

Notes. The significance of the detection based on the separate analysis of the CP and the V^2 is also given. The nature of the detection is either a disk or a point-like source, in which case its main properties are given in the last three columns.

only the best-fitting companion contrast (i.e., minimum χ^2 value) at each position in the search region. The resulting χ^2 map can then be used to derive the probability for the single-star model to adequately represent the data based on the χ^2 distribution under a Gaussian noise assumption. If this probability is below a predefined threshold, the single-star model can be rejected and the best-fit binary solution is then considered as statistically significant. The detection criterion is defined as a threshold on the significance of the detection, which can be translated into a confidence level if the underlying probability distribution function is known.

To determine the significance level to use as a detection threshold, we study the noise properties of the data set by including negative contrasts in our model for the off-axis companions. While nonphysical, negative companions can be used to represent positive fluctuations in the V^2 (i.e., situations where the measured V^2 is higher than the expected V^2 from the photosphere). Negative companions can also be attributed to noise fluctuations in the CP, which can take both positive and negative values. In the following, we associate negative significance levels to negative companions. A histogram of the significance levels for our complete sample is illustrated in Fig. 5, where the range of the plot has been limited to $[-10, 10]$ for the sake of clarity. The negative significance levels in the histogram are purely due to noise fluctuations, and can therefore be used as a reference to study the noise properties of our sample. The absence of significance levels close to zero in the histogram can be explained by the fact that, in presence of noise and because of the limited number of observations, it is generally possible to obtain a better fit to our data sets by inserting a companion somewhere in the field of view than by using a single-star model. Out of the 52 stars in our observed sample, ten show a negative significance level, but none are below -5σ. We therefore decided to use 5σ as our empirical companion detection threshold based on the combined analysis of V^2 and CP. We note that a 4σ threshold would also have been appropriate for this analysis, owing to the distribution of the negative excesses. However, after a more detailed inspection of the closure phases, all the stars with a significance level between 4σ and 5σ actually turned out to be surrounded by extended emission, and not by point-like sources (see below for details on how this inspection was performed).

4.2. Results of the search

Table 2 lists the stars that have a significance level higher than 5σ for the combined χ^2 analysis. HD 31203, HD 80133, HD 106906, and HD 175073 have strong detections, not only in the combined analysis but also in the individual analysis of V^2 and CP. They are therefore identified as bona fide binary stars. The χ^2 maps illustrating the detection of a point-like source in these four data sets are illustrated in Fig. 6. HD 36187 and HD 61005 have a low significance for the CP-only analysis, meaning that the detected excess is identified as being due to extended emission (no evidence for the presence of a point source). For HD 203 and HD 76143, the situation is not as clear, as the detection is at best marginal in the combined and individual analyses. More careful data inspection is required to decide on the nature of the excess. For HD 203, we note that the detection in the V^2 is about twice as significant as in the closure phases. This is a sign that the excess identified in the combined analysis is most probably due to the presence of a disk, which creates a strong signal in the V^2 but not in the CP. For HD 76143, looking at the closure phases signal reveals a global offset from

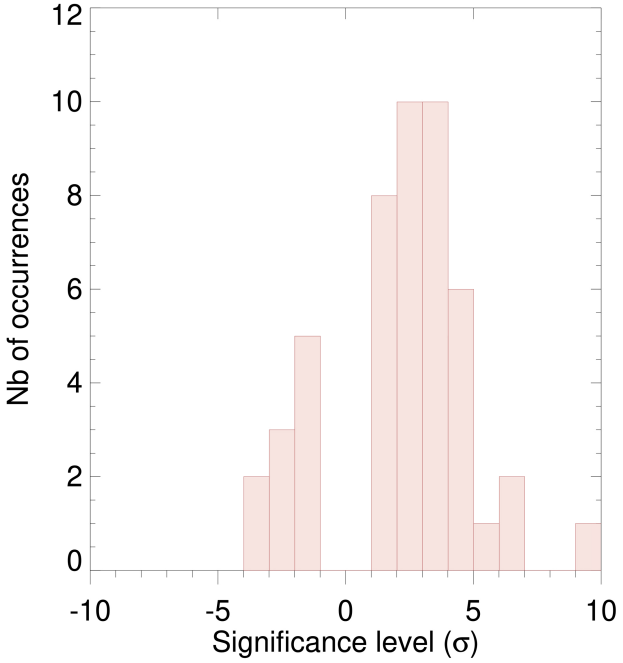

Fig. 5. Statistics of the (signed) significance level for the 52 stars based on the combined χ^2, taking into account the CP and V^2. Four stars with a significance level higher than 10σ are not represented here for the sake of clarity.

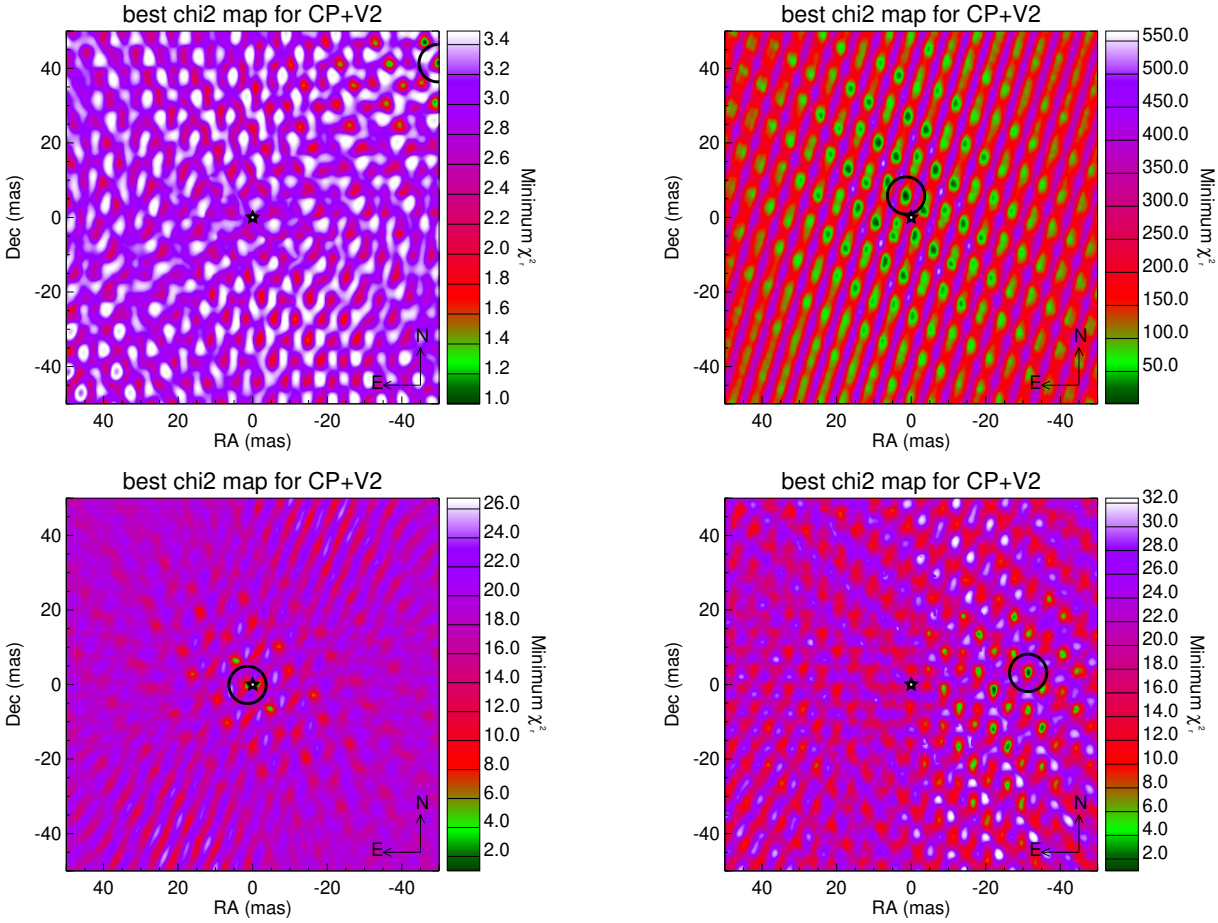

Fig. 6. Normalized χ^2 maps related to the combined CP+V^2 analysis for the four stars showing clear signs of an off-axis companion: HD 31203, HD 80133, HD 106906, and HD 175073 (*from left to right and top to bottom*). The black circles indicate the positions of the minima in the maps.

zero, which is a sign of poor calibration. This poor calibration of the CP is suspected to be at the origin of the (marginal) detection of an excess emission in the CP, and we propose that the most likely explanation is rather the presence of a circumstellar disk (although more observations would be needed to firmly confirm this). This leaves four stars in our sample with previously unknown companions, which will be removed from our search for hot exozodiacal disks. The four new binary stars are described in more detail in the following paragraphs.

4.3. Notes on newly identified companions

HD 31203 (iot Pic A). This F0V-type star is located at 37.1 pc, and is known to be a member of a multiple star system (Tokovinin et al. 2015). The first companion (HD 31204, F4V) is located at 12.″3, and the second one (HD 31261, K2V) at 289″. These companions are well outside the PIONIER field of view, and even outside the AT field of view, and so they do not affect our observations. Besides being a visual multiple system, iot Pic A is known to have variable radial velocities (Nordstrom & Andersen 1985), with a variability larger than 30 km s^{-1} on a timescale of a few days based on four measurements. The nature and orbital parameters of the potential close companion are however not constrained, although the amplitude of the radial velocity (RV) variation points toward a solar-type companion.

Based on the measured contrast $c = 0.04$ and the distance, we estimate that the companion found by our interferometric observations has an absolute magnitude $M_H = 5.49$, which corresponds roughly to a K7V spectral type according to Cox (2000). Assuming a face-on, circular orbit with a semi-major axis of 2.39 au, and a mass of 1.52 $M_\odot$ for iot Pic A (David & Hillenbrand 2015), the orbital period would be around 3 yr. Determining whether this companion corresponds (at least partly) to the source of the RV variability found by Nordstrom & Andersen (1985) would require more RV and interferometric observations.

HD 80133. This K1V-type star is located at 32.8 pc. Based on the measured contrast $c = 0.85$ and the distance, we estimate the companion to have an absolute magnitude $M_H = 4.16$, which corresponds roughly to a G8V spectral type according to Cox (2000). In practice, the measured contrast would rather point to a pair of K1-2V stars, or to a slightly evolved K1IV-V primary with a less evolved G8V secondary, owing to their estimated age of about 13 Gyr (Takeda et al. 2007). Assuming a face-on, circular orbit with a semi-major axis of 0.19 au, and a mass of about 1 $M_\odot$ for HD 80133 (Takeda et al. 2007), the period would be around 1 month. Surprisingly, this star has not been identified as a binary star based on RV measurements, while it was included in the California/Carnegie Planet Search programs (Valenti & Fischer 2005; Takeda et al. 2007). This might be explained either by a (very) poor time coverage in the RV survey, or by a quasi-perfectly face-on orbit. We note that the warm dust disk detected around HD 80133 by Vican & Schneider (2014) is located well outside the estimated semi-major axis of

the companion (beyond 1 au), and should therefore be in a stable circumbinary configuration.

HD 106906. This F5V-type star is located at 92.1 pc, and is identified as a short-period binary in Lagrange et al. (in prep.) based on RV measurements. The interferometric observations presented here confirm the binary nature of the star, which turns out to be a quasi-equal flux binary. Our interferometric observations were included in the analysis of Lagrange et al. (in prep.) to better constrain the orbital parameters of the system. We refer to that paper for a full discussion of this system.

HD 175073. This K1V-type star is located at 24 pc. Based on the measured contrast $c = 0.13$ and the distance, we estimate an absolute magnitude for the companion of $M_H = 6.36$, which corresponds roughly to an M2V spectral type according to Cox (2000). Assuming a face-on, circular orbit with a semi-major axis of 0.76 au, and a mass of 0.8 $M_\odot$ for HD 175073 (Casagrande et al. 2011), the period would be around 9 months. Surprisingly, this star has not been identified as a binary star based on RV measurements, while it was included in previous RV planet surveys according to Grether & Lineweaver (2006). This might be explained either by a (very) poor time coverage in the RV survey, or by a quasi-perfectly face-on orbit. We note that this newly discovered companion cannot be at the origin of the W4 WISE excess detected by Patel et al. (2014) as their analysis was purely based on mid-infrared colors, which are similar for the host star and its companion. We also note that the warm dust disk detected around HD 175073 by Patel et al. (2014) is located well outside the estimated semi-major axis of the companion (beyond 2 au), and should therefore be in a stable circumbinary configuration.

4.4. Sensitivity of PIONIER to faint companions

In the cases where no companion or hot exozodiacal disk are detected around the target stars (35 stars out of the 52 in our sample; see Sect. 5 for a discussion of the hot exozodi detections), we can compute an upper limit on the contrast of faint companions around the target stars as a function of the position in the field of view. These sensitivity maps are derived from the χ^2 analysis, as explained in Absil et al. (2011), with the difference that here we use both the V^2 and the CP in our χ^2 analysis. From the sensitivity maps, we can derive the median sensitivity at a given radial distance by computing the median upper limit along an annulus. The result is illustrated in Fig. 7, where the median sensitivity is plotted as a function of the angular separation for the 35 stars. The typical 5σ sensitivity of PIONIER in "survey mode" (three observing blocks per target) illustrated by the red curve in Fig. 7 is a flux ratio of 0.7% (i.e., $\Delta H = 5.4$) for angular separations larger than 2 mas in the medium-sized AT configuration. This sensitivity corresponds typically to companions with spectral types ranging from M1V to M6V around main sequence stars with spectral types ranging from A0V to K0V.

5. Search for exozodis

After removing the four stars identified as binaries in Sect. 4, we are left with a combined sample of 133 stars, as already described in Sect. 2. Of these 133 stars, 48 are new observations from the observing program described in this paper. In this section, we briefly summarize the principle of the search for hot exozodis, and detail the new exozodis found around our 48 new targets.

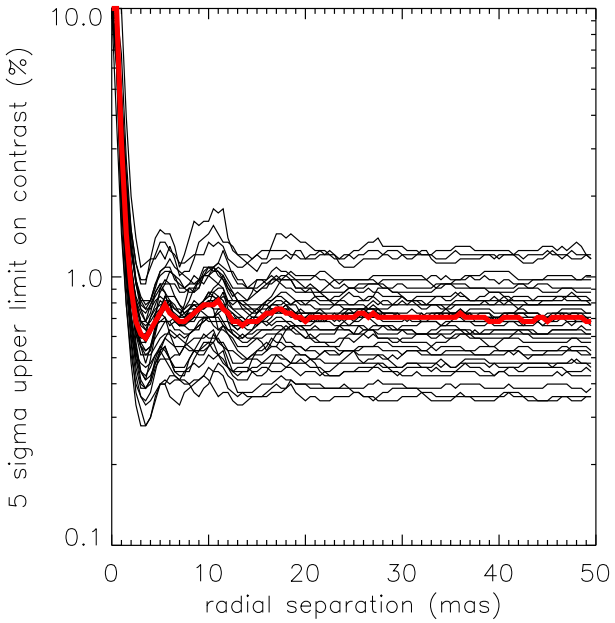

Fig. 7. Sensitivity of PIONIER to point-like companions as a function of the radial distance to the central star for the 35 stars showing no H-band excess in our observations. The sensitivity is expressed as the azimuthal median of the 5σ upper limit based on an analysis of the combined χ^2 for the CP and V^2. The red curve is the median sensitivity on the 35 stars.

When it comes to the detection of faint, circumstellar excess emission, the strength of infrared interferometry is the ability to spatially resolve this emission and thus spatially disentangle it from the much brighter stellar emission. When observing at small baselines of up to a few tens of meters, the host star is nearly unresolved (minimizing the effects of its uncertain diameter on the prediction of the system's V^2), while an extended circumstellar emission is ideally fully resolved (see di Folco et al. 2007). This results in a drop in V^2 compared to the purely stellar V^2, because it adds incoherent flux. This represents the core of our detection strategy.

5.1. Fitting strategy

As shown by previous studies (Absil et al. 2009; Defrère et al. 2011), the V^2 drop induced by a circumstellar disk does not depend significantly on the assumed geometry of the disk, provided that the disk is resolved at the considered baselines. As in previous studies, we therefore consider a model consisting of a limb-darkened photosphere surrounded by a uniform circumstellar emission filling the entire field of view of PIONIER (~400 mas). The visibility expected from a limb-darkened photosphere is estimated according to Hanbury Brown et al. (1974) using the linear H-band limb-darkening coefficients of Claret et al. (1995). We estimate the visibility for the whole bandwidth of each spectral channel, considering the actual spectrum of the star using tabulated H-band spectra from Pickles (1998) and the spectral transmission of the PIONIER instrument. The estimated V^2 are then compared with the measurements, and the flux ratio for each data set is derived. The computation is performed by a set of IDL routines initially developed for CHARA observations by Absil et al. (2006), and later adapted to other interferometers by Defrère et al. (2011). To derive the value and uncertainty of the flux ratio for each target, we use a bootstrapping algorithm, where each individual fit to the data is performed using

a Levenberg-Marquardt least-squares minimization (Markwardt 2009). This means that the individual uncertainties on the data points are not considered directly in the estimate of the uncertainty of the flux ratio, but rather their scatter. In addition, a systematic uncertainty of 5×10^{-4} due to chromaticism is added to the estimated flux ratio (Ertel et al. 2014). For the bootstrapping, we consider that simultaneous spectral channels are fully correlated while the six baselines are fully uncorrelated.

5.2. Results of the search

Table 3 presents the results of the fit in terms of disk-to-star flux ratio, for the 48 new targets observed here. The measured flux ratio is averaged over the three or six spectral channels in our PIONIER observations. To define an appropriate detection threshold, we study the distribution of the significance level χ_f, defined as the ratio between the measured disk/star flux ratio and the uncertainty on this quantity. Figure 8 shows the histogram of the significance level for our sample of 48 stars. We decided to use a threshold of 3σ for the detection as in the study of Ertel et al. (2014). As we used the same methods for observation and data reduction on the same instrument, we can assume that the distribution of the uncertainties will also be comparable. As an additional argument, we study the negative part of the distribution of the significance level. The standard deviation of the negative part, after mirroring it on the positive side, is found to be equal to 1.2. In Fig. 8, a Gaussian distribution with this standard deviation is over-plotted on the data to guide the eye. The good match in shape and width of the distribution confirm that a 3σ criterion is appropriate, which corresponds to a false alarm probability of 0.27%, and should therefore avoid spurious detections in our sample.

The 13 stars highlighted in gray in Table 3 have a significance level above 3σ, and are therefore classified as having a near-infrared circumstellar excess associated with the presence of circumstellar emission. In Fig. 9, we show the wavelength dependence of the measured flux ratio for the 13 stars showing a significant near-infrared excess. The large number of stars with significance levels in the 1σ–3σ range suggests that there may be a population of excesses just below the detection threshold, which remain undetected in our study. Comparing the negative and positive parts of the histogram, we estimate that an additional dozen stars could have an undetected H-band excess in the 1σ–3σ range.

5.3. Notes on specific hot-exozodi targets

HD 4113. This old G5V star is known to have a planetary companion, which was discovered using RV measurements (Tamuz et al. 2008), as well as a directly imaged brown dwarf companion at a projected separation of 22 au (Cheetham et al. 2018). The properties of the inner planetary companion were revisited by Cheetham et al. (2018): $M \sin i = 1.602\ M_{\rm Jup}$, $a = 1.298$ au, $e = 0.8999$. While this star was originally classified as surrounded by a warm dust disk by Vican & Schneider (2014), this classification was based on a single WISE photometric data point at 22 µm. Our revised SED analysis does not show the presence of any significant dust population around this star, based on WISE and AKARI photometry. The presence of a hot dust population therefore does not seem to be connected to a massive outer reservoir of larger bodies. It is interesting to assess whether its inner, eccentric giant planet may have a direct influence on the architecture of the hot dust population. We assume that most of the hot dust is located at the sublimation distance of silicate grains (sublimation temperature of 1500 K), that is, at a distance of 0.04 au. Based on the orbital elements of the planets, the periastron is at 0.12 au, while the apastron is at 2.42 au. This orbital configuration suggests that the planet could have a direct influence on the architecture of the dust disk. To our knowledge, this is only the second hot dust system with a well-characterized

Table 3. Summary of the results for the 48 stars used for our new hot exozodiacal disk survey (excluding all binaries, and the data sets removed in Sect. 3).

Star	Contrast (%)	Signif. (σ)	χ^2_r
HD 203	0.96 ± 0.23	4.25	0.84
HD 2834	2.29 ± 0.85	2.69	5.69
HD 3126	-0.01 ± 0.24	−0.04	0.63
HD 4113	0.75 ± 0.20	3.82	0.63
HD 9672	0.30 ± 0.31	0.96	1.85
HD 10269	-0.16 ± 0.14	−1.15	0.31
HD 10939	0.35 ± 0.33	1.05	1.11
HD 15427	0.05 ± 0.18	0.28	0.46
HD 17848	1.21 ± 0.14	8.69	0.37
HD 23484	0.69 ± 0.25	2.71	0.74
HD 24649	1.14 ± 0.23	5.05	0.80
HD 28287	0.06 ± 0.32	0.19	1.36
HD 29137	0.23 ± 0.16	1.45	0.66
HD 36187 [(a)]	1.95 ± 0.13	15.00	0.40
HD 37306	0.26 ± 0.15	1.75	0.49
HD 37484	0.28 ± 0.21	1.36	0.84
HD 38949	-0.09 ± 0.18	−0.51	0.71
HD 41278	0.40 ± 0.22	1.85	0.68
HD 44524	0.01 ± 0.20	0.05	0.66
HD 60491	0.44 ± 0.16	2.78	0.61
HD 61005	0.81 ± 0.12	6.70	0.36
HD 71722	0.37 ± 0.17	2.21	0.57
HD 76143	0.60 ± 0.18	3.33	0.47
HD 80883	1.43 ± 0.18	8.07	0.65
HD 89886 [(a)]	0.92 ± 0.26	3.47	1.02
HD 90781	0.63 ± 0.16	3.98	0.41
HD 90874	0.34 ± 0.13	2.62	0.36
HD 92945	0.00 ± 0.18	0.00	0.51
HD 105850	-0.06 ± 0.18	−0.34	0.56
HD 105912	0.31 ± 0.15	2.08	0.45
HD 109573	0.35 ± 0.15	2.35	0.39
HD 109704	0.85 ± 0.12	7.03	0.34
HD 112603	0.41 ± 0.25	1.61	0.84
HD 117716	0.40 ± 0.18	2.26	0.44
HD 118972	0.16 ± 0.09	1.70	0.16
HD 136544	1.43 ± 0.35	4.04	1.16
HD 141943	-0.15 ± 0.19	−0.76	0.51
HD 161612	-0.30 ± 0.12	−2.48	0.30
HD 174474	-0.12 ± 0.20	−0.61	0.75
HD 179520	0.44 ± 0.24	1.79	0.76
HD 181327	0.48 ± 0.16	3.03	0.45
HD 185615	-0.61 ± 0.31	−1.94	0.92
HD 191089	0.33 ± 0.48	0.68	2.29
HD 192758	0.12 ± 0.28	0.42	0.89
HD 196141	0.39 ± 0.20	1.99	0.58
HD 205674	0.43 ± 0.50	0.86	2.52
HD 220476	0.04 ± 0.18	0.23	0.49
HD 224228	0.27 ± 0.39	0.69	0.98

Notes. Stars showing a significant level of excess emission (significance higher than 3σ) are highlighted in gray. The reduced χ^2 of the star+disk model fit to the data is given in the last column. [(a)]Not used in the statistical analysis due to insufficient mid- to far-infrared data.

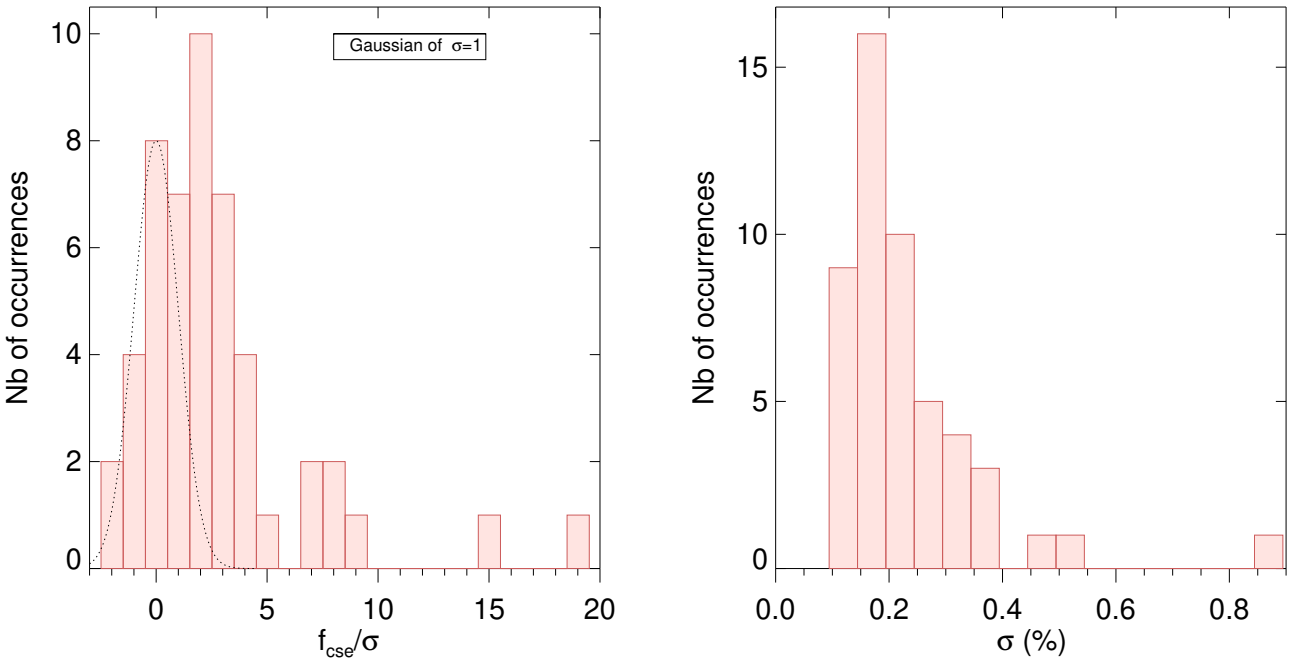

Fig. 8. Distribution of the excess significance level (*left*) and of the uncertainties on the disk-to-star flux ratio (*right*) for the observed sample. The Gaussian fit to the negative part of the significance distribution is represented by a dotted line.

inner giant planet (the first one being β Pictoris). This configuration could be used to constrain the origin of the hot dust. Because of the presence of the planet, Poynting-Robertson (P-R) drag acting on dust grains from a hypothetical (warm or cold) outer dust belt that would remain below the detection threshold is unlikely to efficiently replenish the hot disk, as already suggested in a more general case by van Lieshout et al. (2014) and by Bonsor et al. (2018) based on numerical simulations. A scenario where planetesimals belonging to an outer reservoir would be destabilized by the RV planet and sent towards the inner, hot regions where they would sublimate seems like a more plausible hot-dust-production scenario in this case, in a process somewhat akin to the falling-evaporating-bodies scenario proposed for the β Pictoris system (Beust et al. 1990) – although such a massive planet would be better at ejecting planetesimals than scattering them inwards (e.g., Wyatt et al. 2017).

HD 20794. The near-infrared excess detected around this nearby Solar-type star was already reported in Ertel et al. (2014). This star is known to be the host of at least three (maybe four) super-Earth planets, orbiting between 0.1 and 1 au from the star (Feng et al. 2017), and may also host a massive giant planet at a separation of between 2 and 10 au based on *Gaia* proper motion analysis (Kervella et al. 2019). Based on our SED analysis, and on the detailed model described in Kennedy et al. (2015), we do not confirm the presence of a warm dust population as suggested by Cotten & Song (2016), and classify this target as a cold disk system with a temperature of 80 K. It is another case where a planetary system is located between the hot, inner disk and the outer debris disk, as discussed in detail by Kennedy et al. (2015). Even only considering the RV planets orbiting around HD 20794, which are much less massive than the Jupiter-sized companion of HD 4113, the planetary system is still expected to largely prevent dust from replenishing the inner disk through P–R drag. This is another indication that P–R drag is probably not at the origin of – or at least not the only contributor to – the detected near-infrared excess.

HD 61005 and HD 181327. These two stars are known to be surrounded by copious amounts of dust, and show asymmetries in their outer debris disk, which might be due to collision of Pluto-like objects. HD 61005 is also found by our SED analysis to include a warm dust population at a blackbody temperature of ~120 K. Based on near-infrared scattered light observations, Olofsson et al. (2016) and Esposito et al. (2016) show that the eastern side of the HD 61005 disk is brighter than the western side. Olofsson et al. (2016) argue that an observed peak of density at the pericenter of the disk may be the signpost of a recent impact, because the material released by the impact would pass again through the initial collision point, creating more collision and thus enhancing the density. HD 181327, a member of the β Pic moving group (~20 Myr), also shows an asymmetry in its outer disk, which may be caused by a recent massive collisional event or by interactions with the interstellar medium (Stark et al. 2014b). The possible collisional activity in the outer part of these two debris disks could be related to a major dynamical instability akin to the Large Heavy Bombardment in our Solar system. In such an event, we would expect planetesimals to be injected in the inner parts of the planetary system, where they may create the hot dust detected in our observations.

HD 109573 (HR 4796). This A0-type member of the TW Hya association (~10 Myr) does not show a significant H-band excess when considering the three PIONIER spectral channels together. However, analysis of the spectral channels separately reveals a strong slope of the excess emission, increasing with wavelength to a level such that the longest channel has an excess of $0.51\% \pm 0.17\%$, significant at the 3σ level (see Fig. 9). This may correspond to the onset of thermal emission of a hot exozodiacal disk at a temperature of around 1000 K. Although tentative, this possible H-band excess is interesting to put in perspective with the global debris disk architecture. According to Chen et al. (2014), the debris disk can be best represented by a two-temperature blackbody model, with the innermost ring at a temperature of 231 K (i.e., at about 5.7 au from the star). We

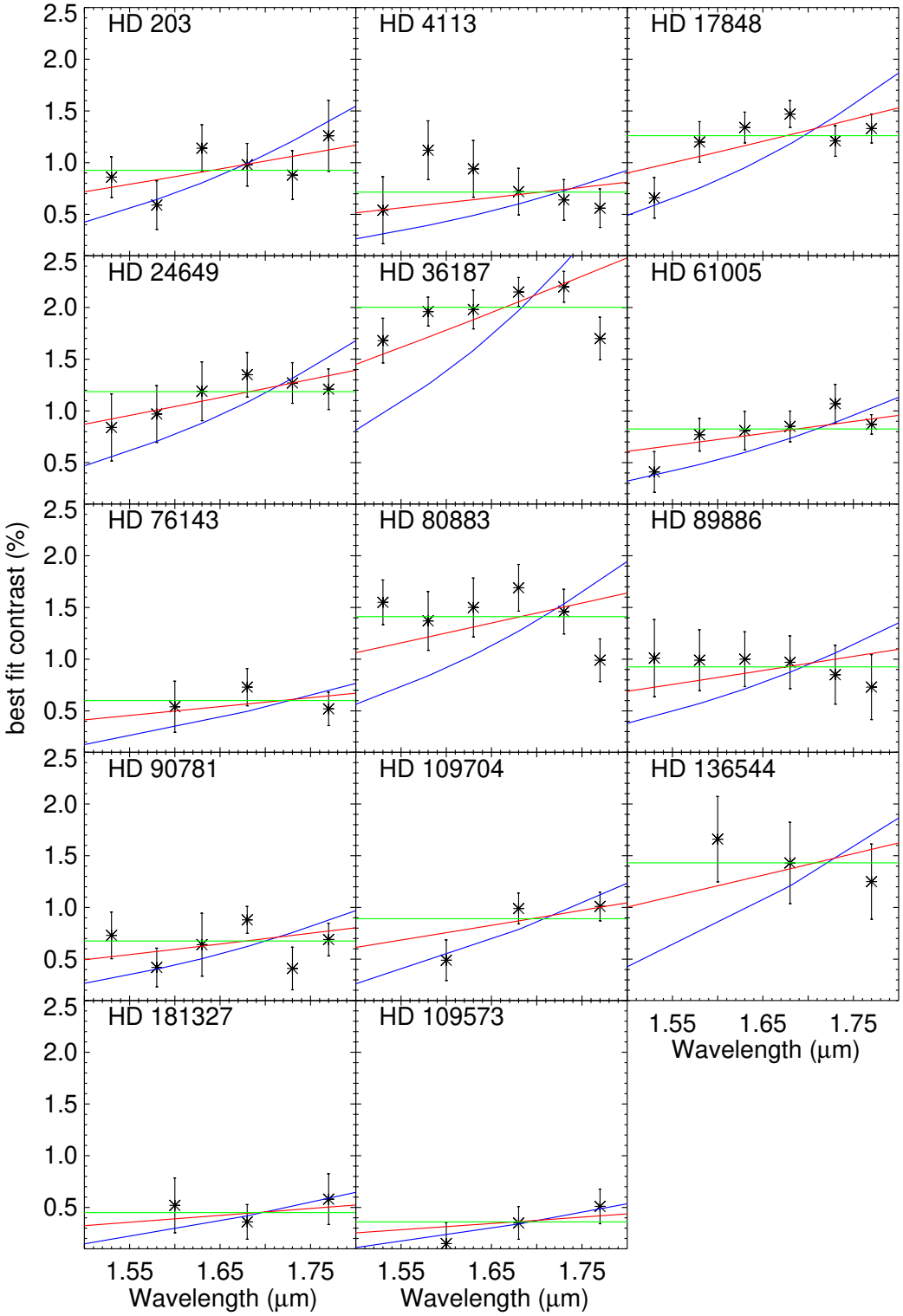

Fig. 9. Disk-to-star flux ratio as a function of wavelength for the 13 targets showing a significant H-band excess in our observations, as well as for HD 109573 (HR 4796), which shows a significant excess only in the reddest spectral channel. The blue, red, and green curves show the best fit to these measured flux ratios using blackbodies at 1000 K, 2000 K, and at the temperature of the star (constant flux ratio), respectively.

note however that the presence of warm dust in this system is disputed. Indeed, Wahhaj et al. (2005) found evidence of warm dust based on mid-infrared imaging, but Kennedy & Wyatt (2014) proposed that the emission of HR 4796 is compatible with a single blackbody. A single blackbody is also suggested by our SED analysis, with a temperature of 97 K, which results in a cold dust classification in our statistical sample. More recently, Lisse et al. (2017) suggested the presence of a tenuous thermal emission component from close-in, ~850 K circumstellar material based on near- to mid-infrared spectroscopy, which might be directly connected to the small H-band excess detected in our PIONIER data.

Near-infrared high-contrast imaging shows that the outer belt around HR 4796 consists of a sharp, offset ring of dust (e.g.,

Table 4. Hot exozodiacal disk statistics from the combined PIONIER surveys of Ertel et al. (2014) and this work.

	A-type stars			F-type stars			G/K-type stars			Total		
	#S	#E	Detect. rate	#S	#E	Detect. rate	#S	#E	Detect. rate	#S	#E	Detect. rate
All[(a)]	40	7	$17.5^{+7.5}_{-4.4}$%	51	10	$19.6^{+6.7}_{-4.4}$%	42	5	$11.9^{+6.8}_{-3.3}$%	133	22	$16.5^{+3.7}_{-2.7}$%
Warm dust	18	3	$16.7^{+12.1}_{-5.3}$%	11	2	$18.2^{+16.3}_{-6.4}$%	6	1	$16.7^{+23.2}_{-6.3}$%	35	6	$17.1^{+8.1}_{-4.6}$%
Warm dust only	12	2	$16.7^{+15.5}_{-5.8}$%	7	2	$28.6^{+20.3}_{-10.6}$%	5	0	$0.0^{+26.3}_{-0.0}$%	24	4	$16.7^{+10.1}_{-5.0}$%
Cold dust only	5	2	$40.0^{+21.4}_{-15.6}$%	12	2	$16.6^{+15.5}_{-5.8}$%	14	1	$7.1^{+13.2}_{-2.3}$%	31	5	$16.1^{+8.6}_{-4.5}$%
No warm dust	21	3	$14.3^{+10.8}_{-4.6}$%	39	7	$17.9^{+7.7}_{-4.5}$%	36	4	$11.1^{+7.4}_{-3.2}$%	96	14	$14.6^{+4.3}_{-2.8}$%
No dust	16	1	$6.3^{+11.8}_{-2.0}$%	27	5	$18.5^{+9.6}_{-5.2}$%	22	3	$13.6^{+10.4}_{-4.3}$%	65	9	$13.8^{+5.4}_{-3.2}$%

Notes. Columns "#S" and "#E" represent the number of target stars and of hot exozodi detections, respectively. [(a)]Also includes two dusty stars that have no warm or cold classification: HD 36187 (A0V) and HD 89886 (F7V).

Milli et al. 2017; Chen et al. 2020) with an angular separation from the star of as small as ∼200 mas along the semi-minor axis due to projection effects. The detected H-band excess may therefore also be (partly) due to the contribution of scattered light from the outer debris disk. Based on the surface brightness of the disk extracted by Milli et al. (2017), and considering the off-axis transmission of the PIONIER single-mode fibers, we estimate that the outer disk could contribute up to 0.1% in terms of integrated H-band excess. The outer disk alone would therefore most probably not explain the measured excess of ∼0.5%. Another piece of evidence for that is the tentative slope in the measured excess, which would not be consistent with scattered light.

The morphology of the HR 4796 outer disk can be best explained through the influence of an eccentric planetary companion that would clear the interior region of the cold dust belt (Lagrange et al. 2012). Both Perrin et al. (2015) and Milli et al. (2017) suggest that the main contribution to scattered light in the outer dust ring comes from rather large, porous grains. This points towards a low dynamical excitation in the outer disk (Lisse et al. 2017), which seems at odds with the main scenarios proposed to explain the presence of a hot exozodiacal disk. Once again, the hot dust population seems disconnected from the cold dust reservoir, but before investigating the global disk architecture further, follow-up observations with near-infrared interferometry will be needed to confirm the tentative H-band excess.

6. Discussion

In Table 4, we summarize the results of the PIONIER surveys for hot exozodis presented here and in Ertel et al. (2014), in terms of the number of detections and detection rates. The results are separated by spectral type, and as a function of the presence of detectable amounts of warm and/or cold dust populations. A graphical representation of the most important information of this table is shown in Fig. 10, and forms the basis of the discussion in the following paragraphs.

6.1. Correlation between hot and warm dust

In our warm dust sample, we measure a detection rate of $17.1^{+8.1}_{-4.6}$% for H-band excesses, while the control sample with no warm dust shows a detection rate of $14.6^{+4.3}_{-2.8}$%. These two occurrence rates are well within their respective error bars, and we

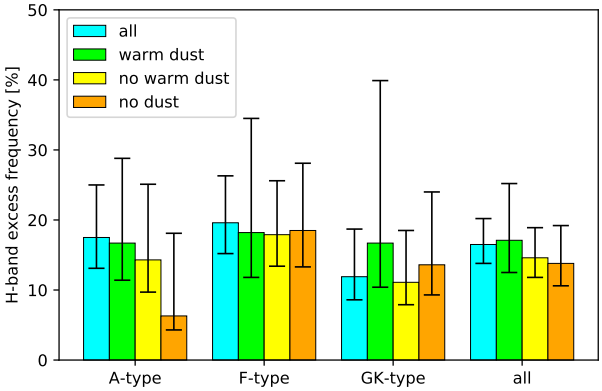

Fig. 10. Detection rate of hot exozodiacal dust as a function of spectral type, and as a function of the presence of a known warm dust reservoir. No significant difference in detection rate is found between the various populations.

note that choosing any temperature threshold in the 100–200 K range to distinguish warm from cold dust populations would not change this conclusion. In order to confirm that this result is compatible with the two samples being drawn from the same population, we performed a two-sample Anderson-Darling test, which tests the null hypothesis that two samples are drawn from the same population, without having to specify the distribution function of that population. Here, the two samples are defined as the collection of the H-band excess levels in the warm dust and control samples, regardless of their spectral type. The two-sample test returns a p-value of 0.13, which confirms that the null hypothesis cannot be rejected. Performing the Anderson-Darling test on the significance of the H-band excess instead of the excess level itself in order to account for the specific sensitivity level reached on each star does not change the conclusion, with a p-value of 0.22. This is consistent with the findings of Mennesson et al. (2014), who used the mid-infrared Keck Interferometer Nuller (KIN) to search for warm dust around 11 stars already known to host hot excesses from near-infrared interferometric observations (among a total KIN sample of 40 stars), and did not find a significant correlation between the presence of hot and warm dust. The same conclusion was reached by the recent analysis of the Large Binocular Telescope Interferometer (LBTI) HOSTS survey (Ertel et al. 2018, 2020), which is based on a sample of 38 stars. This lack of correlation is understood as the telltale sign of a disconnection between hot

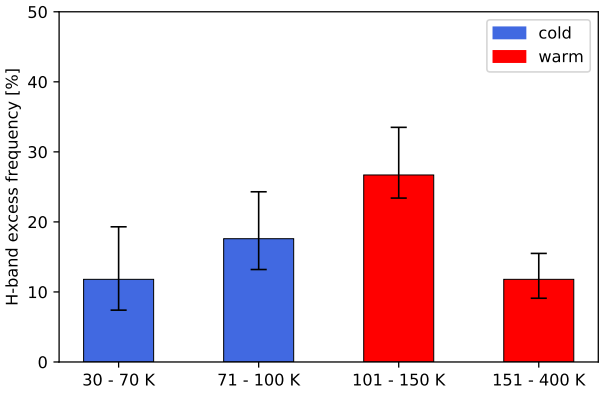

Fig. 11. Occurrence rate of H-band excesses for the 66 stars hosting a known dust reservoir, as a function of the estimated temperature of the dust.

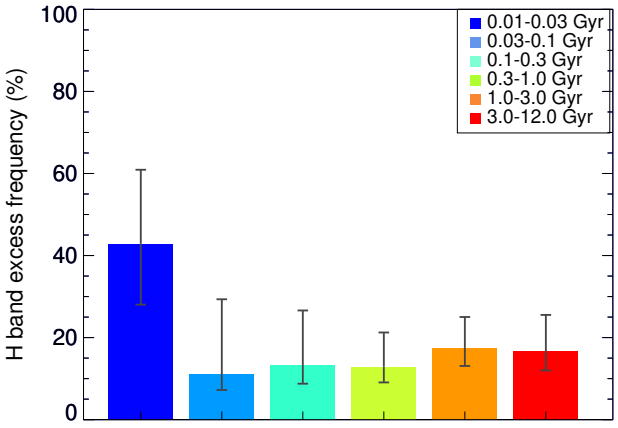

Fig. 12. Occurrence rate of H-band excesses as a function of stellar age in the combined sample of 133 stars.

and warm dust populations, which would then not be created by the same parent bodies. Here, with our much larger sample (131 stars), we confirm that the detection rate of hot dust is not significantly enhanced by the presence of a warm asteroid belt. While it cannot be excluded that warm asteroid belts act as prominent suppliers of material to replenish the short-lived hot dust population, the presence of large amounts of warm dust does not seem to be a pre-requisite to the presence of hot exozodiacal dust, and we confirm that hot dust should not be considered as the bright, near-infrared counterpart of warm belts (or at least not in a directly connected way). This conclusion is of course only valid at the sensitivity level of the instruments used in this study (both regarding near-infrared interferometry and mid- to far-infrared spectrophotometry), and may be challenged by future, more sensitive observations.

To refine our analysis, we also investigated the possible correlation between the temperature of the outer dust reservoirs and the detection of an H-band excess. If there is a direct connection between inner and outer dust disks, we may expect that the warmer the outer disk, the higher the chances of detecting an H-band excess. However, Fig. 11 indicates a lack of correlation between the temperature of the outer dust reservoir and the occurrence rate of H-band excesses, the apparent drop in occurrence rate for the warmest dust reservoirs being statistically insignificant. A more relevant way to carry out this analysis may be to use the expected warm belt location rather than its temperature. As the dust temperature is a good proxy for its location when taking into account the blackbody correction of Pawellek & Krivov (2015) as discussed in Sect. 2.1, this does not change the conclusion. A last possible correlation that we investigated is between the luminosity of the warm debris disk (as a proxy for its mass) and the H-band excess. The inward flux of dust due to P–R drag is indeed expected to scale (albeit weakly) with the mass of the warm dust disk (Kennedy & Piette 2015). No correlation was found here either, which seems to concur with the conclusions of Sezestre et al. (2019) that P–R drag is unlikely to be at the origin of the hot exozodi phenomenon, although we recognize that fractional luminosities may not be directly proportional to the dust mass. Finally, our new results also make it possible to revisit the conclusion of Ertel et al. (2014) that the presence of hot dust does not correlate with the presence of cold dust. We confirm this conclusion by comparing the detection rate of H-band excesses around the "cold dust only" (no warm dust) and "no dust" samples (see Table 4), and find them to be fully compatible within the statistical uncertainties.

6.2. Occurrence rate versus stellar parameters

Previous studies suggested that hot exozodiacal dust is more frequent around early-type stars than solar-type stars, although no firm conclusion could be drawn because of the limited sample (Absil et al. 2013; Ertel et al. 2014). Here, this correlation no longer appears to be as clear, with A-type stars showing a similar detection rate ($17.5^{+7.5}_{-4.4}$%) to FGK-type stars ($16.1^{+4.5}_{-3.1}$%) in the combined sample. This result may seem to contradict the prediction of the magnetic trapping model, which is shown by Rieke et al. (2016) to be more efficient around rapidly rotating stars. Although a measurement of $v \sin i$ is not available for all of the stars of our sample, we consider that stars with spectral type earlier than F5 have a much higher chance of showing high rotational velocities, because of the absence of a strong convective layer to brake their initial rotation. A two-sample Anderson-Darling test comparing the H-band excess levels of hot exozodis around stars earlier and later than F5 shows that there is a 2.5% probability of them being drawn from the same population, which suggests, at a 2.2σ level, that the two samples are drawn from different populations. The same Anderson-Darling test performed on the excess significance instead of the excess levels shows a 5.3% probability of them being drawn from the same population, marginal evidence at best.

In the previous section, we show that there is a lack of correlation between the presence of inner (hot) dust and outer (warm/cold) dust in our combined sample of 133 stars. To investigate whether this lack of correlation holds when looking separately at different spectral types, we performed the same two-sample Anderson-Darling test as before, considering early-type stars and solar-type stars separately. We chose to set the boundary between early-type and solar-type stars at F5, which corresponds to the spectral type where strong convective envelopes start to appear. The probability of the null hypothesis turns out to be above 0.3 in both cases, which suggests once again that the distribution of H-band excesses does not have a different behavior around stars with and without warm dust.

Based on 85 single stars in their PIONIER survey, Ertel et al. (2014) investigated the possible relationship between stellar age and hot exozodi detection rate, revealing the absence of a correlation, although a possible trend was observed, namely that FGK stars could have more frequent hot exozodis at old ages. We revisit their analysis including the 48 new single stars observed here (see Fig. 12). Based on this larger sample of young main sequence stars, we note an increase in detection rate at very

young ages, with three stars out of five within the β Pic moving group (~20 Myr) showing a hot exozodi in the combined sample. Furthermore, among the two stars from the β Pic moving group showing no hot exozodi, HD 172555 was identified as a marginal H-band detection by Ertel et al. (2014) based on the longest wavelength channel, and this detection was later confirmed to be significant through follow-up observations (Ertel et al. 2016). This leads to an actual detection rate of 80^{+8}_{-25}% for hot exozodis at 20 Myr of age. To determine whether the population of young stars is significantly different from the older stars, we performed an Anderson-Darling test on two samples: the first one composed of young stars (younger than 30 Myr) and the second composed of the other stars. We find a probability of 6.8% that the two samples are drawn from the same population, which is marginal evidence that they are issued from different populations, at a 1.8σ level. Although this trend is based on a very small sample, it fits well within the picture that young main sequence stars might still be in the process of forming terrestrial planets, which may lead to strong dust production rates even in the innermost parts of the planetary systems. Nevertheless, it is somewhat puzzling that the youngest star in our sample (HD 109573 or HR 4796, part of the TW Hya association), only shows a marginal H-band excess (0.35 ± 0.15%).

6.3. Influence of partly resolved exozodis

An important aspect of the hot exozodi detection statistics, which was not explored in previous works, is the influence of the location of the dust on its detectability with infrared interferometry. The most critical case in terms of angular resolution is for the most compact disks, which corresponds to the case where the circumstellar emission comes mostly from a region close to the sublimation distance of the dust grains. This situation indeed corresponds to our current picture of hot exozodi detected with near-infrared interferometry, for which the measured excesses are understood to originate from the thermal emission of hot grains at a temperature close to sublimation (e.g., Mennesson et al. 2011; Lebreton et al. 2013). The emission could be even more confined by physical mechanisms such as grain pile-up (Kobayashi et al. 2009), magnetic trapping (Rieke et al. 2016), or gas drag (Pearce et al. 2020). In this case, the circumstellar emission might only be partly resolved by the interferometer, which would decrease the strength of the visibility drop, especially at the shortest baselines. Partly resolving the hot exozodiacal disk would therefore lead to a decreased sensitivity, as only part of the disk emission would affect the measured V^2. Here, we explore how the uneven sensitivity to compact hot exozodis around our target stars could bias the results of our survey.

So far, our working hypothesis has always been that circumstellar disks are fully resolved, and we have modeled them as a uniform emission filling the whole field of view. To test the impact of this working hypothesis on the measured detection rates, we computed the sublimation radius of the grains for each of the 133 stars in our combined sample, assuming silicates with a sublimation temperature of 1500 K. Our estimation of the sublimation radius is based on a simple blackbody assumption, which we validated by running specific simulations with the GRaTeR radiative transfer package (Augereau et al. 1999; Lebreton et al. 2012) to explore the dependency of the sublimation radius on grain size and composition. The resulting sublimation radii are given in Table B.3.

The estimated sublimation radii must then be compared with the angular resolution of the interferometric array to determine whether the disks are fully or only partly resolved. To do so, we considered infinitesimally thin rings with diameters ranging between 1.2 and 8.5 mas, corresponding to twice the minimum and maximum sublimation distance for the newly observed stars on the medium-sized AT configuration (see Table B.3). We injected these thin rings around a typical star of our survey to produce the expected V^2 for the star–disk system, using the medium-sized AT configuration at the VLTI (D0-H0-G1-I1) and a typical observing setup in terms of target elevation and hour angle coverage. This expected V^2 was then passed to our exozodi detection routine, which is based on the assumption of a fully resolved circumstellar disk filling the entire field of view, and we extracted the measured disk-to-star flux ratio using our standard fitting method. This measured flux ratio was then compared to the actual flux ratio injected in the model (chosen to be 3% in this case), to produce a "sensitivity reduction factor" (ϕ), defined as the ratio of measured to injected disk-to-star flux ratio. The result of this exercise is illustrated in Fig. 13, where we plot the sensitivity reduction factor for thin annular disks of increasing diameter. As expected, smaller disk diameters lead to a greater drop in sensitivity, with only about 15% of the flux detected for the most compact disks. Half of the flux is missed for a disk diameter of about 2.5 mas (i.e., disk radius of 1.25 mas). The same exercise was carried out on the compact AT configuration (A1-B2-C1-D0) for the sample observed by Ertel et al. (2014). The resulting sensitivity reduction factor ϕ is given for all of the stars in our combined sample in Table B.3, where asterisks denote the stars observed on the medium-sized AT configuration within the observing program presented in this paper.

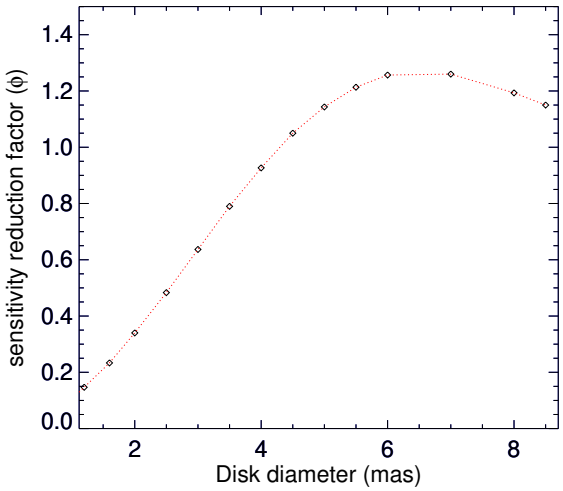

Fig. 13. Sensitivity reduction factor (i.e., ratio between the measured and injected flux ratio) as a function of the diameter of the circumstellar ring, for the medium-sized AT configuration (D0-H0-G1-I1).

Knowing the sensitivity reduction factor for all the stars in the PIONIER surveys, we can compute the effective sensitivity ($\sigma_{\rm eff}$) of our observations under the new working hypothesis that all the disks are confined to the sublimation radius of silicates. The effective sensitivity, defined as the 1σ error bar on the disk-to-star flux ratio divided by the sensitivity reduction factor, is given in Table B.3. Based on these revised sensitivities, we define a homogeneous sample in terms of effective sensitivity, by rejecting all the stars that have an effective sensitivity of greater than 0.5% (for which the chances of detecting a hot exozodi are much lower owing to the typical brightness of hot exozodis). This gives us a new sample of 68 stars, among which 25 show the presence of warm dust. The hot exozodi detection rate can then be recomputed on this new, more homogeneous sample, which is

Table 5. Hot exozodiacal disk statistics from the combined PIONIER surveys (Ertel et al. 2014, and this work), after removing all stars showing an effective sensitivity of greater than 0.5%, taking into account partial resolution effects.

	A-type stars			F-type stars			G/K-type stars			Total		
	#S	#E	Detect. rate	#S	#E	Detect. rate	#S	#E	Detect. rate	#S	#E	Detect. rate
All[a]	34	7	$20.6^{+8.5}_{-5.2}$%	28	7	$25.0^{+9.7}_{-6.3}$%	6	1	$16.7^{+23.2}_{-6.3}$%	68	15	$22.1^{+5.8}_{-4.2}$%
Warm disk	16	3	$18.8^{+13.1}_{-6.1}$%	8	2	$25.0^{+19.3}_{-9.1}$%	1	1	$100^{+0.0}_{-60.0}$%	25	6	$24.0^{+10.3}_{-6.4}$%
Warm disk only	11	2	$18.2^{+16.3}_{-6.4}$%	6	2	$33.3^{+21.1}_{-12.7}$%	0	0	N.A.	17	4	$23.5^{+12.7}_{-7.1}$%
Cold disk only	4	2	$50.0^{+20.2}_{-20.2}$%	6	2	$33.3^{+21.1}_{-12.7}$%	2	0	$0.0^{+45.7}_{-0.0}$%	12	4	$33.3^{+15.1}_{-10.3}$%
No warm disk	17	3	$17.6^{+12.6}_{-5.7}$%	20	5	$25.0^{+11.7}_{-7.1}$%	5	0	$0.0^{+26.3}_{-0.0}$%	42	8	$19.0^{+7.4}_{-4.6}$%
No disk	13	1	$7.7^{+14.0}_{-2.6}$%	14	3	$21.4^{+14.2}_{-7.0}$%	3	0	$0.0^{+36.8}_{-0.0}$%	30	4	$13.3^{+8.6}_{-4.0}$%

Notes. Columns "#S" and "#E" represent the number of target stars and of hot exozodi detections, respectively. [(a)]Also includes one dusty star with no warm or cold classification: HD 36187 (A0V).

however strongly biased towards early-type stars because of the larger star–disk angular separation in those systems. The new detection rates are summarized in Table 5. They are still compatible with each other within error bars, although the occurrence rate for the "no-dust" sample ($13.3^{+8.6}_{-4.0}$%) seems to be systematically lower than for the rest of the sample (stars hosting warm and/or cold dust), which shows an occurrence rate of $28.9^{+8.2}_{-6.1}$% (11 out of 38 stars[3]). To further explore this possible correlation, we used a two-sample Anderson-Darling test to compare the H-band excess distribution within the dusty and nondusty samples, containing respectively 38 and 30 stars. The Anderson-Darling test on the H-band excess levels shows that the null hypothesis that the two samples are drawn from the same population can be rejected at significance level $p = 0.0028$, which corresponds to a 3.0σ level. Using the excess significance instead of the excess levels in the Anderson–Darling test would increase the significance level to 3.4σ that the two samples are drawn different populations. As the 1σ sensitivity threshold of 0.5% used to define our sensitivity-corrected sample is somewhat arbitrary, we also examine a case where the threshold is set to 0.33%. This new threshold boosts the significance that a common underlying population can be rejected to a 3.7σ level, for a sample of 40 stars. Tentative evidence for a correlation between the presence of hot dust and an outer reservoir was already found based on K-band observations at the CHARA array, but only for solar-type stars (FGK types), and based on a smaller sample (Absil et al. 2013; Nuñez et al. 2017). This tentative correlation was not confirmed at H band on a larger sample of stars in the study of Ertel et al. (2014). The analysis presented here seems to finally reconcile the trends observed at H and K bands, and provides the first evidence at a $>3\sigma$ level that the presence of an outer dust reservoir may have a significant influence on the appearance of a near-infrared excess across all spectral types, although we underline the fact that this conclusion is based on the assumption that the dust is arranged in a thin ring close to its sublimation radius, and that the samples are still relatively small. It must also be kept in mind that the absence of observable amounts of warm or cold dust populations does not mean the complete absence of outer dust reservoirs, which could artificially increase or decrease the significance of this tentative correlation.

[3] This includes one dusty star for which the dust temperature could not be determined, meaning that it does not show up in either the "warm" or "cold" dust categories in Table 5.

6.4. Location and temperature of the hot dust

In order to further investigate the robustness of the tentative conclusion from the previous section, an interesting question is whether we could discriminate between a fully resolved (uniform) circumstellar emission and a thin annulus model. This type of morphological study has already been attempted on Fomalhaut by Absil et al. (2009) using VLTI/VINCI, and on β Pictoris by Defrère et al. (2012) using VLTI/PIONIER. In both cases, a very large number of observations were available, but no constraint could be derived on the disk morphology. We do not expect this situation to change in the present case, where we only collected three observing blocks on each of our targets. Nevertheless, we search for possible signs of partly resolved disks in our whole sample of detected hot exozodis by looking for a slope in the V^2 drop as a function of baseline. Indeed, partly resolved disks should lead to a smaller V^2 drop at shorter baselines, as they become less and less resolved. This exercise is illustrated in Fig. 14 for the case of HD 80883, for which the expected sublimation radius is particularly small. The data set shows no significant slope, suggesting that the excess is more likely to be caused by an extended disk than by a thin ring at the sublimation radius, although both models are consistent with the available data set.

Another possible way to constrain the location of the dust grains would be to infer their temperature. This can potentially be done by exploring the wavelength dependence of the measured disk-to-star flux ratio. To test this, we fitted blackbodies of various temperatures – including the host star temperature (flat contrast) to simulate the effect of scattered light – to the measured disk-to-star flux ratio as a function of wavelength (Fig. 9). Blackbody models with temperatures between 1500 K and the host star temperature fit the data almost equally well, with a reduced χ^2 of around 1. Using a blackbody temperature of 1000 K increases the median reduced χ^2 to about 2 for our sample of 13 hot exozodis. The accuracy that can currently be reached with precision infrared interferometers such as VLTI/PIONIER is therefore not high enough to conclude on the dust temperature. At best, we could reject the hypothesis that the detected excesses are due to the thermal emission of grains at temperatures below 1000 K, which is not expected as such grains would not produce a significant H-band emission anyway. A possible way to circumvent this limitation would be to follow up our detections at other wavelengths, for instance using the second generation interferometric instruments of the VLTI (GRAVITY

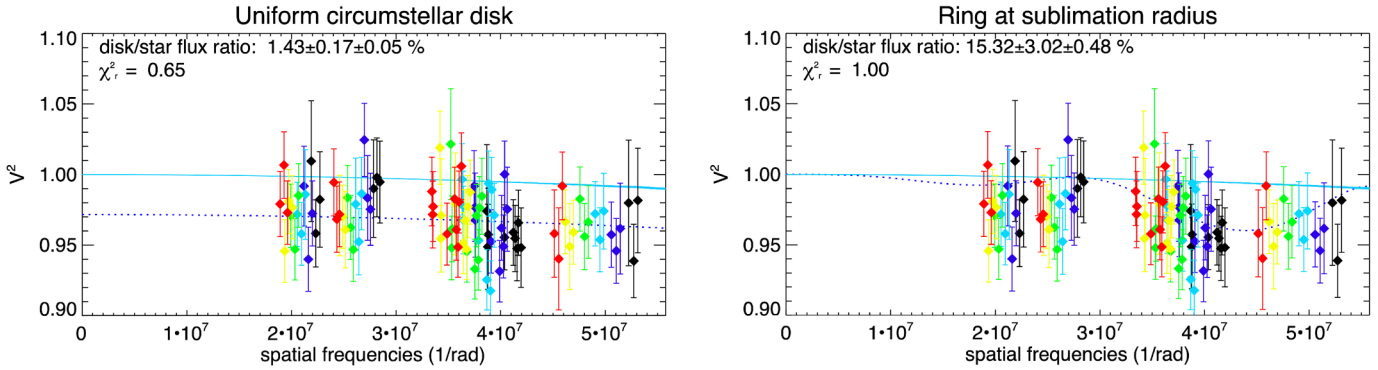

Fig. 14. Measured and modeled squared visibilities for HD 80883 using a limb-darkened star surrounded by uniform circumstellar emission (*left*) or by a ring of dust at the sublimation radius (*right*). The different colors of the data points represent the different spectral channels (one color per channel). The solid blue line shows the expected visibility for the stellar photosphere alone, and the dotted blue line the best fit for the star + disk model. Both disk models provide a reasonable fit to the measured visibilities, with $\chi^2_r \leq 1$.

in the near-infrared and MATISSE in the mid-infrared; see e.g., Kirchschlager et al. 2020).

6.5. Origin of the hot dust

The lack of a strong correlation between the hot exozodi phenomenon and the amount of warm and/or cold dust in outer reservoirs remains puzzling. Our understanding is that the hot dust is likely supplied from an outer reservoir for most stars, because parent bodies cannot survive on million-year timescales close to the dust sublimation radius because of collisional activity (e.g., Absil et al. 2006). However, the determining factor of whether detectable amounts of hot dust are present seems not to be the mass or location of this reservoir, but rather a different condition triggering the phenomenon. Trapping mechanisms have been proposed to sustain the observed, high dust masses that would otherwise require extreme replenishment rates because of the efficient removal of the hot dust (e.g., Pearce et al. 2020). These mechanisms include the pile up of sublimating dust (Kobayashi et al. 2009), the effect of the stellar magnetic field (Czechowski & Mann 2010; Rieke et al. 2016), or the effect of gas (Lebreton et al. 2013; Pearce et al. 2020), possibly originating in the sublimation of the dust grains themselves. Trapping mechanisms could explain why even faint, undetected outer belts can supply sufficient material to produce detectable hot dust. Alternatively, or in addition, a specific configuration of the dust reservoir and a planetary system could be required to supply sufficient material to the inner regions (Bonsor & Wyatt 2012; Bonsor et al. 2012, 2014; Faramaz et al. 2017). Such a mechanism could also be so efficient that we cannot distinguish between its action on systems with detectable or undetectable cold reservoirs.

Irrespective of the delivery mechanism and of the presence or absence of a trapping mechanism, a larger reservoir of cold material provides more material to be delivered to the inner region. Therefore, naively one would still expect a correlation between the presence of a massive debris disk and near-infrared excess, at least statistically if not for individual targets. There is only weak evidence for this to be the case in our sample, with a tentative correlation appearing only after correcting the sample for sensitivity under the assumption that all the hot dust is located close to the sublimation distance of silicates (Sect. 6.3). The lack of a more prominent correlation between hot dust and outer reservoirs might imply that there is an upper limit on the amount of hot dust that may be present or be supplied, and that this is reached in systems where the conditions for delivery and trapping are met, even for relatively small outer reservoirs. In the case of P–R drag, the amount of dust that reaches the innermost regions is limited by collisions between the migrating dust grains (Wyatt 2005): while massive, collision-dominated outer belts produce more dust that can be dragged inward, most of this dust is destroyed before it reaches the inner regions. In contrast, most of the dust created in more tenuous, transport-dominated outer belts may reach the inner regions. This naturally decouples, to some degree, the amount of dust supplied to the hot exozodi region from the mass of the outer reservoir. For other scenarios, like comet delivery of the hot dust, an upper limit on the amount of hot dust could be set by the collisional evolution of the dust, which happens on a shorter timescale for more massive disks, meaning that an equilibrium between dust influx and removal could typically be reached around similar dust levels. It is also possible that the amount of material transported inwards is dominated by the efficiency of the transport process (e.g., scattering) rather than the supply of material, which would also result in a (partial) decoupling of the hot dust quantity from the brightness of the cold reservoir. Finally, some trapping mechanisms may have intrinsic upper limits on the amount of dust they can trap. An alternative explanation for the similar flux ratios observed around all stars with near-infrared excess would be that the hot dust is optically thick. In that case, the observed flux would be driven by the surface area of the disk, and would be independent of the dust mass to first order. This scenario would then require the surface area of the hot disk to increase for earlier spectral types, which could at least partly be explained by the larger dust sublimation radius around earlier spectral types.

Among the potential origins for the hot dust population, the possibility that hot dust is primordial (i.e., a remnant of the initial protoplanetary disk) cannot be completely ruled out without a detailed analysis of the possible trapping mechanisms. However, this would require the trapping mechanism at play to be efficient enough on gigayear timescales, and to be ongoing since the late stages of the primordial disk dispersal, which seems rather unlikely. This scenario would also be expected to show a more prominent age dependence in the hot exozodi phenomenon.

The apparent lack of correlation between hot and warm dust populations could be both an asset and a drawback in the preparation of space-based missions dedicated to Earth-like planet imaging. On one hand, the lack of correlation means that stars hosting hot dust populations should not necessarily be removed from the potential target lists of such missions, because they

are not necessarily associated with large amounts of warm dust in the habitable zone. However, the influence of hot dust populations located at much smaller angular separation from the star than the habitable zone on mission performance remains to be investigated, a task that we defer to a future, dedicated study. On the other hand, the lack of correlation also means that the detection of significant near-infrared emission with precision interferometry is not a prime criterion to build the target lists, which means that more mid-infrared interferometric observations with existing (LBTI/NOMIC, Ertel et al. 2020) or upcoming (VLTI/Hi-5, Defrère et al. 2018) instruments will be needed.

7. Conclusions

In this study, we used the VLTI/PIONIER interferometric instrument to search for resolved near-infrared circumstellar emission around a sample of main sequence stars known to harbor a warm dust disk from previous mid-infrared spectrophotometric observations in an attempt to identify a possible connection between warm and hot dust populations. To this end, we built a target list of 62 stars that showed signs of warm dust in the literature. Among the 52 stars for which we obtained data of sufficient quality, we identified 17 new H-band excesses, among which four are shown to be due to the presence of a previously unknown close stellar companion. The remaining 13 excess are thought to originate from hot dust populations, adding to the nine hot exozodi systems already detected with PIONIER by Ertel et al. (2014). Combining these two samples, resulting in a total of 133 stars, we find an overall detection rate of $16.5^{+3.7}_{-2.7}$% for H-band excesses around nearby main sequence stars, with the possible hint of a larger underlying population of excesses below our sensitivity limit. Taking into account the fact that some of the hot exozodiacal disks may only be partly resolved by our interferometric baseline lengths, we estimate that the true occurrence rate could in reality be as high as $22.1^{+5.8}_{-4.2}$%, if we only include stars that have a corrected 1σ sensitivity of 0.5% or better on the disk-to-star flux ratio. However, our data sets do not allow us to discriminate between a fully resolved disk and a thin annulus at the sublimation radius as the most appropriate model to reproduce our observations, meaning that the true occurrence rate at our sensitivity level could be anywhere between 16.5% and 22.1%.

We then searched for a possible correlation between the presence of a known warm dust population around the target stars and the detection of a near-infrared excess in our interferometric observations. To this aim, we re-evaluated the presence of warm and/or cold dust around all of the 133 stars in our combined sample through SED modeling, and defined two samples: one containing stars showing warm dust emission and one containing stars not showing such emission. We found that the distribution of near-infrared excesses around the warm dust sample is fully compatible with that of the control sample, suggesting the absence of a direct connection between warm and hot dust populations. This conclusion does not depend on the considered spectral type. No correlation was found either between the detection rate of near-infrared excess and stellar age, although there is a marginal trend for young stars ($\lesssim$30 Myr) to have more frequent H-band excesses. After correcting the sensitivity of our observations for the fact that the hot dust could be arranged in a thin ring around its sublimation radius, and subsequently limiting our sample to the stars for which the corrected 1σ error bar is smaller than 0.5%, we find tentative evidence at the 3σ level that the distribution of near-infrared excesses around stars showing any kind of outer dust reservoir (warm or cold) is statistically different from the distribution of near-infrared excesses around stars showing no outer dust reservoir, with larger near-infrared excesses around the dusty stars. This conclusion pertains mostly to early-type (A and F) stars, which make up the majority of our sensitivity-corrected sample, and only holds if the dust is arranged in a thin annulus close to its sublimation radius, a hypothesis that we cannot confirm or rule out based on our PIONIER data. A possible caveat to these conclusions is that some of the near-infrared excesses might be variable, as suggested by Ertel et al. (2016) and Nuñez et al. (2017), meaning that a nondetection does not necessarily mean that there is never any detectable excess around a particular star. It must also be kept in mind that we can only probe correlations down to the sensitivity level of both the near-infrared interferometric observations and the mid- to far-infrared photometry used in this study, and that underlying correlations may exist at lower sensitivity levels.

Although the present work brings to light a tentative correlation between hot and warm or cold dust populations, it does not settle the question of the origin of hot exozodiacal dust. Our current understanding is that at least one transport mechanism is at play to inject material into the innermost parts of planetary systems, and that the material additionally needs to be confined close to its sublimation radius by a trapping mechanism. However, the nature of these transport and trapping mechanisms is still unclear, and will probably require new diagnostic tools to be properly constrained, although it is worth noting that some specific hot-dust systems in our sample appear to be incompatible with P–R drag dust production. High-contrast interferometric observations in the thermal infrared (L, M, and N bands) would be a powerful way to derive useful new constraints on these dust populations.

Acknowledgements. The authors thank the French National Research Agency (ANR, contract ANR-2010 BLAN-0505-01, EXOZODI) for financial support. L.M. acknowledges the F.R.S.-FNRS for financial support through a FRIA PhD fellowship. G.M.K. is supported by the Royal Society as a Royal Society University Research Fellow. J.O. acknowledges support by ANID, – Millennium Science Initiative Program – NCN19_171, from the Universidad de Valparaíso, and from Fondecyt (grant 1180395). We thank the Belgian GTO on VISA for the generous allocation of observing time. This work made use of the Smithsonian/NASA Astrophysics Data System (ADS) and of the Centre de Données astronomiques de Strasbourg (CDS).

References

Absil, O., di Folco, E., Mérand, A., et al. 2006, A&A, 452, 237
Absil, O., di Folco, E., Mérand, A., et al. 2008, A&A, 487, 1041
Absil, O., Mennesson, B., Le Bouquin, J.-B., et al. 2009, ApJ, 704, 150
Absil, O., Le Bouquin, J.-B., Berger, J.-P., et al. 2011, A&A, 535, A68
Absil, O., Defrère, D., Coudé du Foresto, V., et al. 2013, A&A, 555, A104
Allard, F., Homeier, D., & Freytag, B. 2012, Phil. Trans. Roy. Soc. London Ser. A, 370, 2765
Augereau, J. C., Lagrange, A. M., Mouillet, D., Papaloizou, J. C. B., & Grorod, P. A. 1999, A&A, 348, 557
Ballering, N. P., Rieke, G. H., Su, K. Y. L., & Montiel, E. 2013, ApJ, 775, 55
Beust, H., Lagrange-Henri, A. M., Madjar, A. V., & Ferlet, R. 1990, A&A, 236, 202
Binks, A. S., & Jeffries, R. D. 2014, MNRAS, 438, L11
Bonfanti, A., Ortolani, S., & Nascimbeni, V. 2016, A&A, 585, A5
Bonsor, A., & Wyatt, M. C. 2012, MNRAS, 420, 2990
Bonsor, A., Augereau, J. C., & Thébault, P. 2012, A&A, 548, A104
Bonsor, A., Raymond, S. N., Augereau, J.-C., & Ormel, C. W. 2014, MNRAS, 441, 2380
Bonsor, A., Wyatt, M. C., Kral, Q., et al. 2018, MNRAS, 480, 5560
Booth, M., Kennedy, G., Sibthorpe, B., et al. 2013, MNRAS, 428, 1263
Carpenter, J. M., Bouwman, J., Mamajek, E. E., et al. 2009, ApJS, 181, 197
Casagrande, L., Schönrich, R., Asplund, M., et al. 2011, A&A, 530, A138
Chauvin, G., Lagrange, A.-M., Bonavita, M., et al. 2010, A&A, 509, A52

Cheetham, A., Ségransan, D., Peretti, S., et al. 2018, A&A, 614, A16
Chen, C. H., Sargent, B. A., Bohac, C., et al. 2006, ApJS, 166, 351
Chen, C. H., Mittal, T., Kuchner, M., et al. 2014, ApJS, 211, 25
Chen, C., Mazoyer, J., Poteet, C. A., et al. 2020, ApJ, 898, 55
Ciardi, D., van Belle, G. T., Akeson, R. L., & Thompson, R. R. 2001, in BAAS, Vol. 33, American Astronomical Society Meeting Abstracts, 1508
Claret, A., Diaz-Cordoves, J., & Gimenez, A. 1995, A&AS, 114, 247
Cotten, T. H., & Song, I. 2016, ApJS, 225, 15
Cox, A. N., ed. 2000, Allen's astrophysical quantities (Springer)
Cutri, R. M., Skrutskie, M. F., van Dyk, S., et al. 2003, 2MASS All Sky Catalog of point sources
Czechowski, A., & Mann, I. 2010, ApJ, 714, 89
David, T. J., & Hillenbrand, L. A. 2015, ApJ, 804, 146
De Rosa, R. J., Patience, J., Wilson, P. A., et al. 2014, MNRAS, 437, 1216
Defrère, D., Absil, O., den Hartog, R., Hanot, C., & Stark, C. 2010, A&A, 509, A9
Defrère, D., Absil, O., Augereau, J.-C., et al. 2011, A&A, 534, A5
Defrère, D., Stark, C., Cahoy, K., & Beerer, I. 2012, in Proc. SPIE, 8442, Space Telescopes and Instrumentation 2012: Optical, Infrared, and Millimeter Wave, 84420M
Defrère, D., Absil, O., Berger, J. P., et al. 2018, Exp. Astron., 46, 475
Delgado Mena, E., Israelian, G., González Hernández, J. I., et al. 2014, A&A, 562, A92
Delgado Mena, E., Bertrán de Lis, S., Adibekyan, V. Z., et al. 2015, A&A, 576, A69
Desidera, S., Covino, E., Messina, S., et al. 2015, A&A, 573, A126
di Folco, E., Absil, O., Augereau, J.-C., et al. 2007, A&A, 475, 243
Dikarev, V. V., & Schwarz, D. J. 2015, A&A, 584, A9
Durkan, S., Janson, M., & Carson, J. C. 2016, ApJ, 824, 58
Eiroa, C., Marshall, J. P., Mora, A., et al. 2013, A&A, 555, A11
Ertel, S., Absil, O., Defrère, D., et al. 2014, A&A, 570, A128
Ertel, S., Defrère, D., Absil, O., et al. 2016, A&A, 595, A44
Ertel, S., Defrère, D., Hinz, P., et al. 2018, AJ, 155, 194
Ertel, S., Defrère, D., Hinz, P., et al. 2020, AJ, 159, 177
Esposito, T. M., Fitzgerald, M. P., Graham, J. R., et al. 2016, AJ, 152, 85
Faramaz, V., Ertel, S., Booth, M., Cuadra, J., & Simmonds, C. 2017, MNRAS, 465, 2352
Feltzing, S., Holmberg, J., & Hurley, J. R. 2001, A&A, 377, 911
Feng, F., Tuomi, M., & Jones, H. R. A. 2017, A&A, 605, A103
Feroz, F., Hobson, M. P., & Bridges, M. 2009, MNRAS, 398, 1601
Fujiwara, H., Ishihara, D., Onaka, T., et al. 2013, A&A, 550, A45
Grether, D., & Lineweaver, C. H. 2006, ApJ, 640, 1051
Hanbury Brown, R., Davis, J., Lake, R. J. W., & Thompson, R. J. 1974, MNRAS, 167, 475
Hillenbrand, L. A., Carpenter, J. M., Kim, J. S., et al. 2008, ApJ, 677, 630
Holmberg, J., Nordström, B., & Andersen, J. 2009, A&A, 501, 941
Howard, R. A., Vourlidas, A., Bothmer, V., et al. 2019, Nature, 576, 232
Huensch, M., Schmitt, J. H. M. M., & Voges, W. 1998, A&AS, 132, 155
Ishihara, D., Onaka, T., Kataza, H., et al. 2010, A&A, 514, A1
Kennedy, G. M., Matrà, L., Marmier, M., et al. 2015, MNRAS, 449, 3121
Kennedy, G. M., & Wyatt, M. C. 2014, MNRAS, 444, 3164
Kennedy, G. M., & Piette, A. 2015, MNRAS, 449, 2304
Kervella, P., Thévenin, F., Di Folco, E., & Ségransan, D. 2004, A&A, 426, 297
Kervella, P., Arenou, F., Mignard, F., & Thévenin, F. 2019, A&A, 623, A72
Kharchenko, N. V., & Roeser, S. 2009, VizieR Online Data Catalog, I/280
Kirchschlager, F., Wolf, S., Krivov, A. V., Mutschke, H., & Brunngräber, R. 2017, MNRAS, 467, 1614
Kirchschlager, F., Ertel, S., Wolf, S., Matter, A., & Krivov, A. V. 2020, MNRAS, 499, L47
Kobayashi, H., Watanabe, S.-i., Kimura, H., & Yamamoto, T. 2009, Icarus, 201, 395
Lagrange, A.-M., Milli, J., Boccaletti, A., et al. 2012, A&A, 546, A38
Le Bouquin, J.-B., Berger, J.-P., Lazareff, B., et al. 2011, A&A, 535, A67
Le Bouquin, J.-B., Berger, J.-P., Zins, G., et al. 2012, in Proc. SPIE, 8445, Optical and Infrared Interferometry III, 84450I
Lebouteiller, V., Barry, D. J., Spoon, H. W. W., et al. 2011, ApJS, 196, 8
Lebreton, J., Augereau, J.-C., Thi, W.-F., et al. 2012, A&A, 539, A17
Lebreton, J., van Lieshout, R., Augereau, J.-C., et al. 2013, A&A, 555, A146
Lisse, C. M., Sitko, M. L., Marengo, M., et al. 2017, AJ, 154, 182
Maire, A.-L., Boccaletti, A., Rameau, J., et al. 2014, A&A, 566, A126
Maldonado, J., Eiroa, C., Villaver, E., Montesinos, B., & Mora, A. 2012, A&A, 541, A40
Mamajek, E. E., & Hillenbrand, L. A. 2008, ApJ, 687, 1264
Marion, L., Absil, O., Ertel, S., et al. 2014, A&A, 570, A127
Markwardt, C. B. 2009, in Astronomical Society of the Pacific Conference Series, Vol. 411, Astronomical Data Analysis Software and Systems XVIII, eds. D. A. Bohlender, D. Durand, & P. Dowler, 251
Marshall, J. P., Cotton, D. V., Bott, K., et al. 2016, ApJ, 825, 124
McDonald, I., Zijlstra, A. A., & Boyer, M. L. 2012, MNRAS, 427, 343
Mennesson, B., Serabyn, E., Hanot, C., et al. 2011, ApJ, 736, 14
Mennesson, B., Millan-Gabet, R., Serabyn, E., et al. 2014, ApJ, 797, 119
Mérand, A., Bordé, P., & Coudé du Foresto, V. 2005, A&A, 433, 1155
Mermilliod, J.-C. 1987, A&AS, 71, 413
Milli, J., Vigan, A., Mouillet, D., et al. 2017, A&A, 599, A108
Mittal, T., Chen, C. H., Jang-Condell, H., et al. 2015, ApJ, 798, 87
Morales, F. Y., Padgett, D. L., Bryden, G., Werner, M. W., & Furlan, E. 2012, ApJ, 757, 7
Nordstrom, B., & Andersen, J. 1985, A&AS, 61, 53
Nuñez, P. D., Scott, N. J., Mennesson, B., et al. 2017, A&A, 608, A113
Olofsson, J., Samland, M., Avenhaus, H., et al. 2016, A&A, 591, A108
Pace, G. 2013, A&A, 551, L8
Patel, R. I., Metchev, S. A., & Heinze, A. 2014, ApJS, 212, 10
Paunzen, E. 2015, A&A, 580, A23
Pawellek, N., & Krivov, A. V. 2015, MNRAS, 454, 3207
Pawellek, N., Krivov, A. V., Marshall, J. P., et al. 2014, ApJ, 792, 65
Pearce, T. D., Krivov, A. V., & Booth, M. 2020, MNRAS, 498, 2798
Pecaut, M. J., & Mamajek, E. E. 2016, MNRAS, 461, 794
Perrin, M. D., Duchene, G., Millar-Blanchaer, M., et al. 2015, ApJ, 799, 182
Pickles, A. J. 1998, PASP, 110, 863
Rieke, G. H., Gáspár, A., & Ballering, N. P. 2016, ApJ, 816, 50
Roberge, A., Chen, C. H., Millan-Gabet, R., et al. 2012, PASP, 124, 799
Sezestre, É., Augereau, J. C., & Thébault, P. 2019, A&A, 626, A2
Sierchio, J. M., Rieke, G. H., Su, K. Y. L., & Gáspár, A. 2014, ApJ, 785, 33
Sibthorpe, B., Kennedy, G. M., Wyatt, M. C., et al. 2018, MNRAS, 475, 3046
Stark, C. C., & Kuchner, M. J. 2008, ApJ, 686, 637
Stark, C. C., Roberge, A., Mandell, A., & Robinson, T. D. 2014a, ApJ, 795, 122
Stark, C. C., Schneider, G., Weinberger, A. J., et al. 2014b, ApJ, 789, 58
Su, K. Y. L., Rieke, G. H., Stansberry, J. A., et al. 2006, ApJ, 653, 675
Takeda, G., Ford, E. B., Sills, A., et al. 2007, ApJS, 168, 297
Tamuz, O., Ségransan, D., Udry, S., et al. 2008, A&A, 480, L33
Tokovinin, A., Pribulla, T., & Fischer, D. 2015, AJ, 149, 8
Tsantaki, M., Sousa, S. G., Adibekyan, V. Z., et al. 2013, A&A, 555, A150
Tucci Maia, M., Ramírez, I., Meléndez, J., et al. 2016, A&A, 590, A32
Valenti, J. A., & Fischer, D. A. 2005, ApJS, 159, 141
van Lieshout, R., Dominik, C., Kama, M., & Min, M. 2014, A&A, 571, A51
Vican, L., & Schneider, A. 2014, ApJ, 780, 154
Wahhaj, Z., Koerner, D. W., Backman, D. E., et al. 2005, ApJ, 618, 385
Wahhaj, Z., Liu, M. C., Nielsen, E. L., et al. 2013, ApJ, 773, 179
Wright, E. L., Eisenhardt, P. R. M., Mainzer, A. K., et al. 2010, AJ, 140, 1868
Wu, C.-J., Wu, H., Lam, M.-I., et al. 2013, ApJS, 208, 29
Wyatt, M. C. 2005, A&A, 433, 1007
Wyatt, M. C., Bonsor, A., Jackson, A. P., Marino, S., & Shannon, A. 2017, MNRAS, 464, 3385
Yelverton, B., Kennedy, G. M., Su, K. Y. L., & Wyatt, M. C. 2019, MNRAS, 488, 3588
Yelverton, B., Kennedy, G. M., & Su, K. Y. L. 2020, MNRAS, 495, 1943
Zuckerman, B., Song, I., & Bessell, M. S. 2004, ApJ, 613, L65

Appendix A: Spectral energy distributions

Figure A.1 shows observations and model spectral energy distribution for each target in our combined sample of 133 stars.

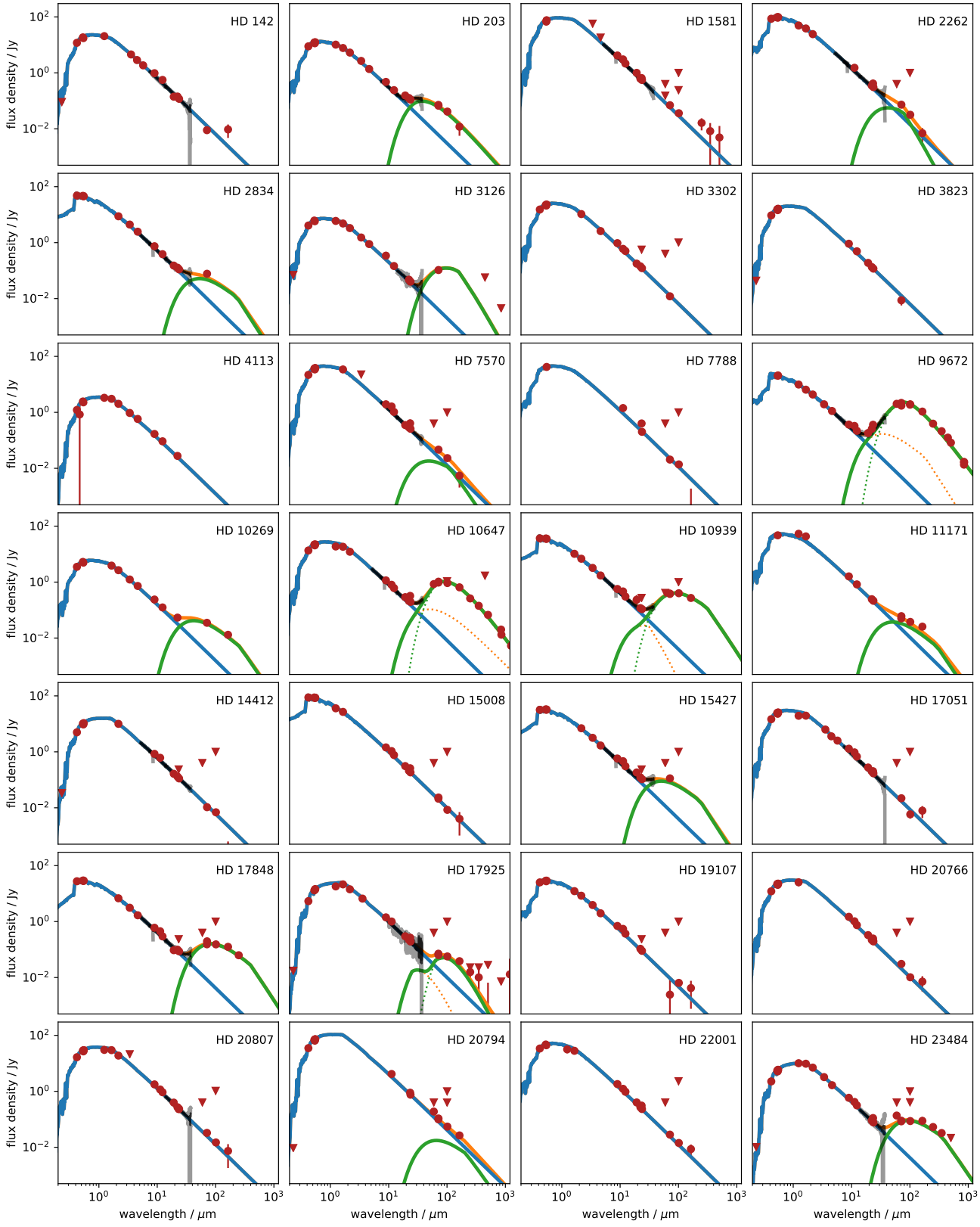

Fig. A.1. Observations and models for the targets in our survey. Each panel shows photometry as dots, upper limits as triangles, and IRS spectra as black lines. Models are shown as solid lines, with blue for the star, green for the disk, and orange for the total model. Where two are fitted, individual disk components are shown as dotted lines.

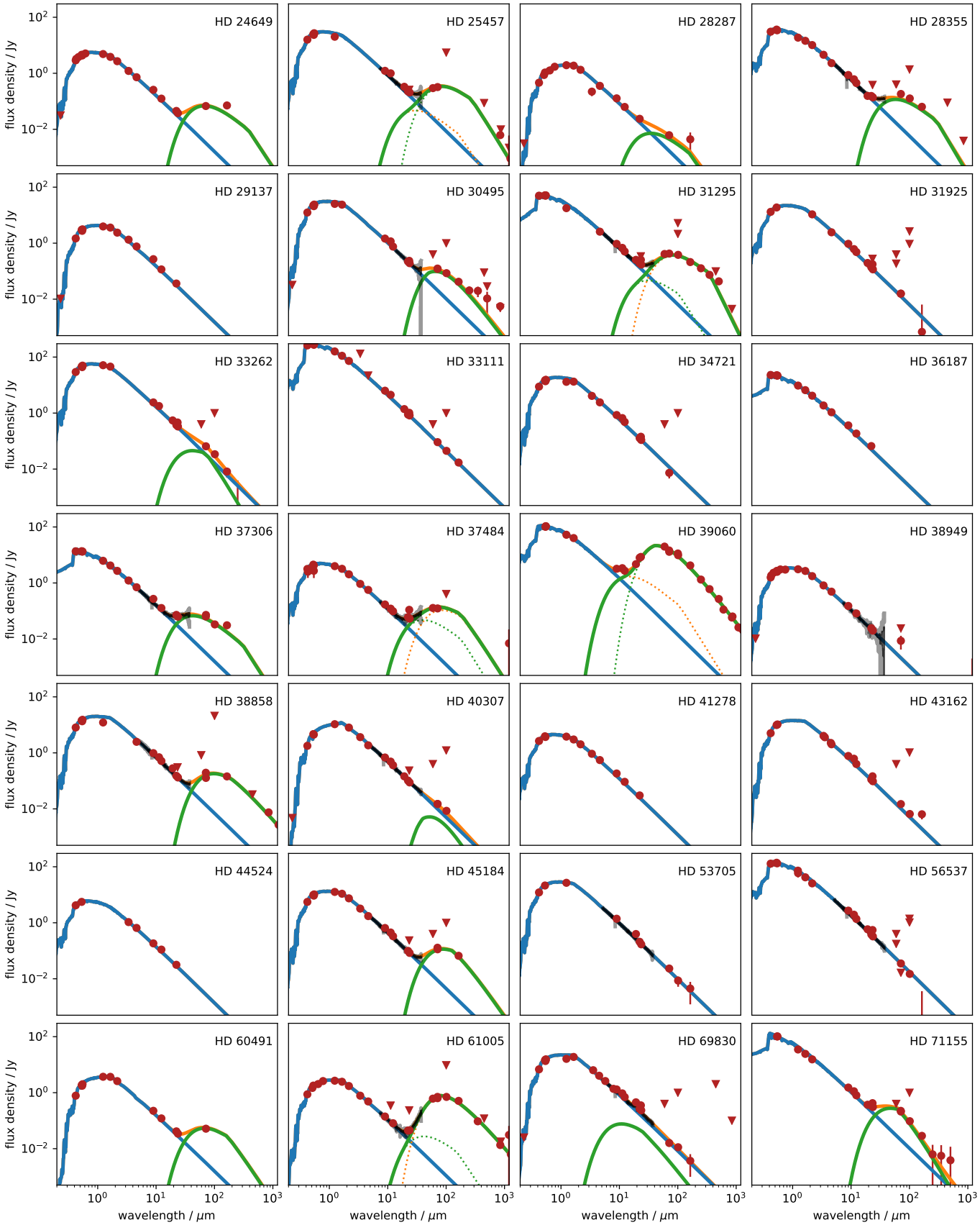

Fig. A.1. continued.

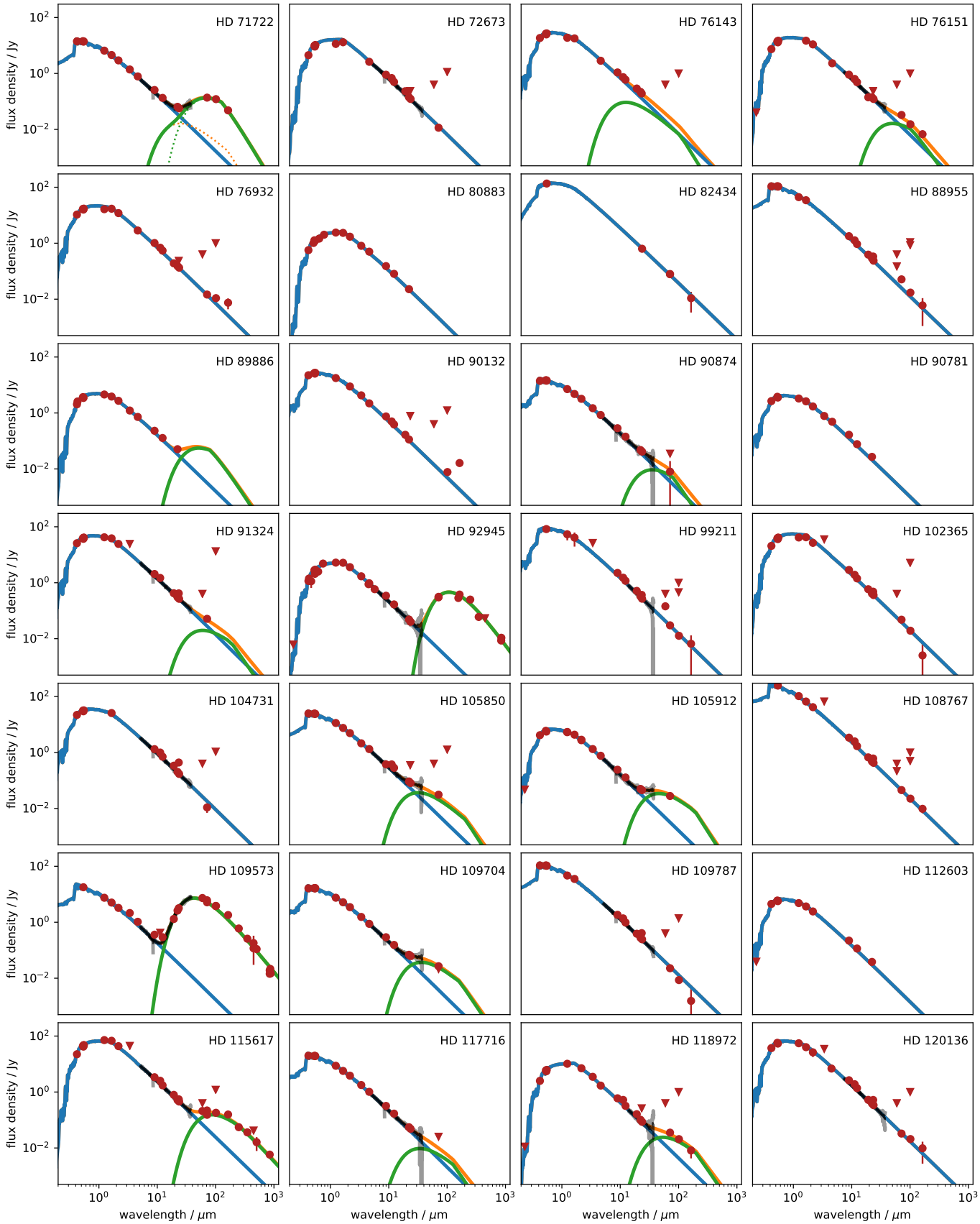

Fig. A.1. continued.

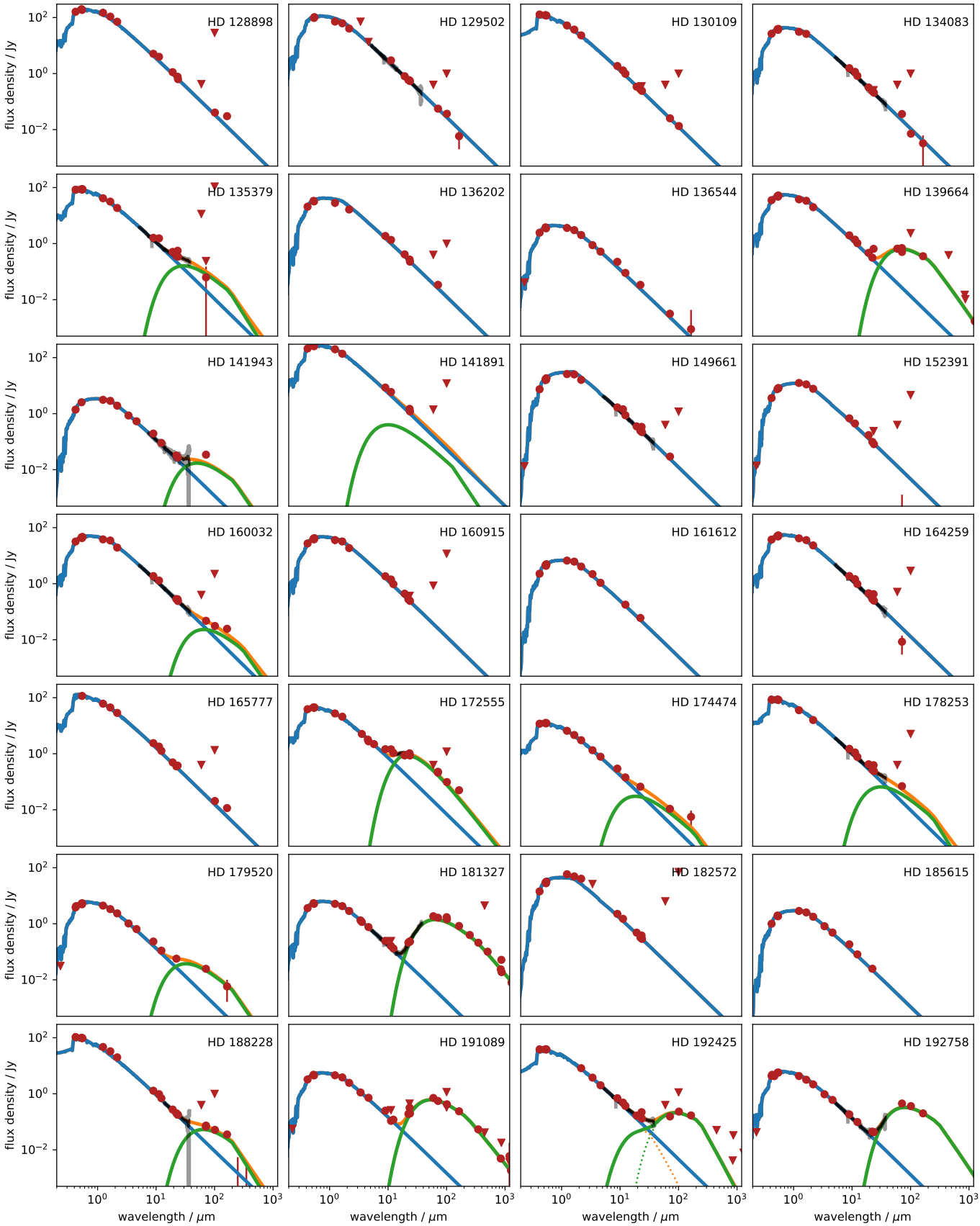

Fig. A.1. continued.

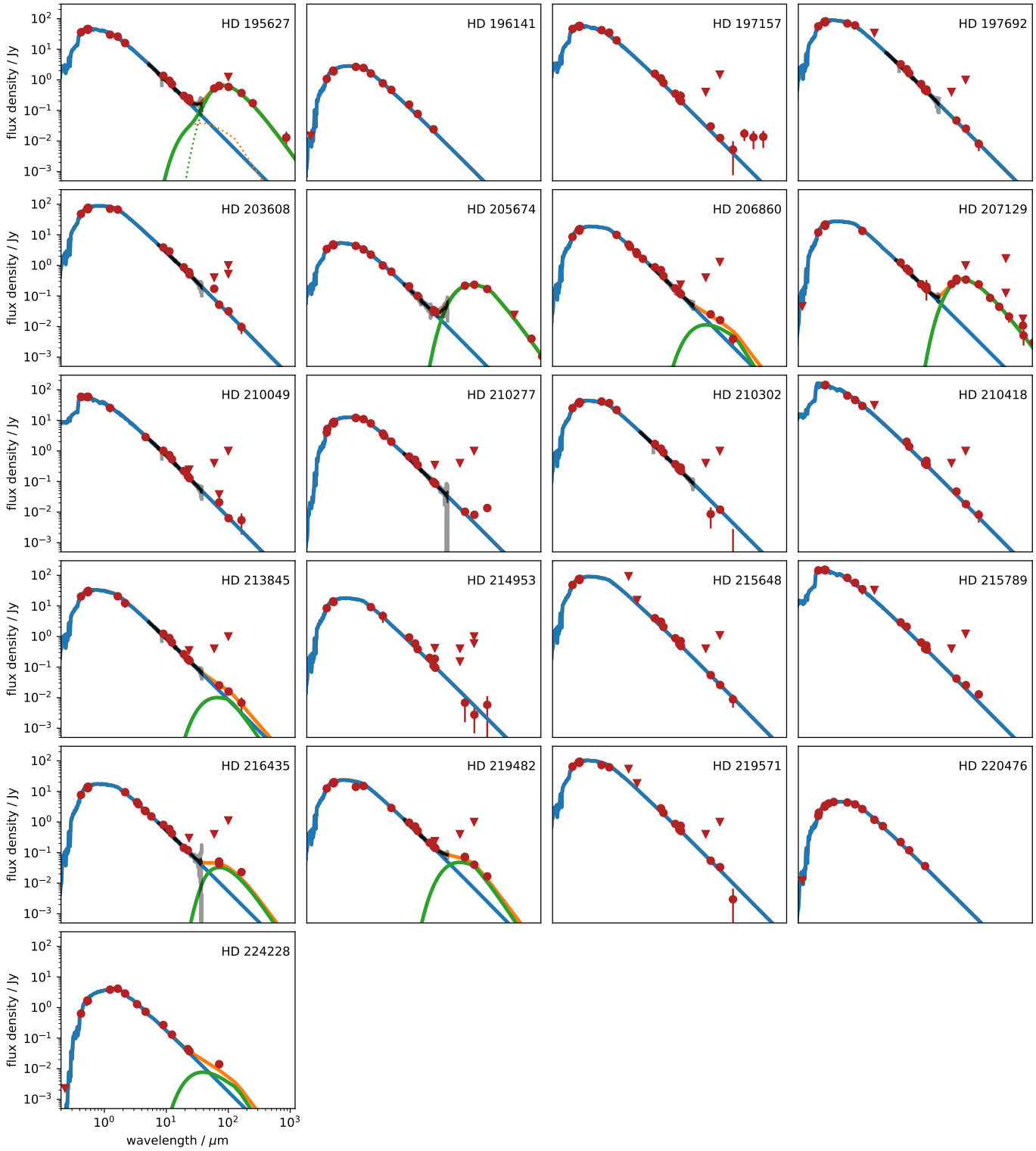

Fig. A.1. continued.

Appendix B: Additional tables

Table B.1. Main properties of the 62 newly observed stars.

Star	Type	Dist. (pc)	V (mag)	H (mag)	θ_{LD} (mas)	Age (Gyr)	References
HD 203	F2IV	39.0	$6.181^{0.003}$	$5.32^{0.05}$	$0.347^{0.005}$	0.021	1, 2, **3**, 31, 32
HD 2834	A0V	53.0	$4.751^{0.008}$	$4.76^{0.07}$	$0.381^{0.006}$	0.22	**1**, 2, 3, 4
HD 3126	F5V	41.0	$6.907^{0.009}$	$5.85^{0.05}$	$0.284^{0.004}$	1.59	**1**, 2, 3, 4
HD 4113	G5V	44.0	$7.889^{0.009}$	$6.34^{0.02}$	$0.240^{0.003}$	5.8	5, **7**
HD 4247	F0V	27.0	$5.218^{0.003}$	$4.46^{0.01}$	$0.513^{0.006}$	1.7	6
HD 9672	A1V	59.0	$5.611^{0.004}$	$5.53^{0.02}$	$0.273^{0.004}$	0.1	**1**, 3, 4, 8
HD 10008	K0/1V	24.0	$7.66^{0.01}$	$5.90^{0.04}$	$0.324^{0.005}$	4.2	1, **3**, 9
HD 10269	F5V	48.0	$7.078^{0.004}$	$5.90^{0.04}$	$0.252^{0.003}$	1.6	**1**, 4
HD 10939	A1V	62.0	$5.033^{0.003}$	$5.03^{0.02}$	$0.339^{0.006}$	0.2	**1**, 2, 3
HD 15427	A2/3V	47.0	$5.124^{0.002}$	$5.03^{0.02}$	$0.349^{0.005}$	0.24	**1**, 2
HD 17848	A2V	50.5	$5.252^{0.004}$	$5.16^{0.08}$	$0.350^{0.005}$	0.28	1, 2, **3**, 4, 8
HD 23484	K1V	16.0	$6.982^{0.004}$	$5.09^{0.02}$	$0.484^{0.006}$	6.9	2, 3, 8, 10, 11
HD 24649	F6V	41.0	$7.217^{0.007}$	$6.09^{0.03}$	$0.261^{0.004}$	4.8	**1**, 6
HD 28287	K0V	38.0	$8.77^{0.01}$	$6.87^{0.04}$	$0.210^{0.003}$	0.1	**1**, 3, 7
HD 29137	G5V	52.0	$7.663^{0.008}$	$6.16^{0.03}$	$0.258^{0.004}$	6.29	**1**, 12
HD 31203	F0IV	37.1	$5.606^{0.004}$	$4.88^{0.02}$	$0.414^{0.006}$	0.70	4, 13
HD 31392	G9V	26.0	$7.600^{0.008}$	$5.89^{0.04}$	$0.317^{0.005}$	3.70	3, **8**
HD 36187	A0V	87.8	$5.557^{0.003}$	$5.51^{0.02}$	$0.264^{0.004}$	0.25	4, **14**
HD 37306	A2V	63.0	$6.087^{0.004}$	$5.992^{0.02}$	$0.215^{0.003}$	0.16	1, **2**, 3, 4, 8
HD 37484	F3V	57.0	$7.249^{0.008}$	$6.29^{0.02}$	$0.217^{0.003}$	0.7	**1**, 2, 3, 6, 8
HD 38949	G1V	43.3	$7.808^{0.008}$	$6.48^{0.04}$	$0.215^{0.003}$	0.9	2, 3, **8**
HD 41278	F5V	56.0	$7.394^{0.008}$	$6.36^{0.03}$	$0.220^{0.003}$	2.3	**1**, 6
HD 43879	F5V	64.1	$7.494^{0.008}$	$6.46^{0.04}$	$0.216^{0.003}$	2.0	4, 15
HD 44524	F3V	102.3	$7.012^{0.01}$	$6.46^{0.03}$	$0.193^{0.003}$	1.6	6, **14**, 15
HD 59967	G3V	21.8	$6.657^{0.004}$	$5.25^{0.02}$	$0.412^{0.006}$	0.63	**1**, 2, 3, 16, 17
HD 60491	K2V	25.0	$8.15^{0.01}$	$6.14^{0.02}$	$0.298^{0.005}$	0.08	**1**, 3, 18
HD 61005	G3/5V	35.3	$8.215^{0.008}$	$6.58^{0.04}$	$0.228^{0.004}$	0.1	**1**, 2, 3, 19
HD 71722	A0V	71.7	$6.05^{0.004}$	$5.91^{0.02}$	$0.225^{0.003}$	0.4	**1**, 2, 3, 4, 8, 20
HD 76143	F5IV	52.0	$5.328^{0.003}$	$4.42^{0.02}$	$0.536^{0.009}$	2.2	**1**, 3, 4
HD 80133	K1/2V	68.5	$7.76^{0.01}$	$5.90^{0.03}$	$0.337^{0.005}$	0.4	**7**, 11
HD 80883	K0V	36.2	$8.59^{0.01}$	$6.63^{0.05}$	$0.242^{0.004}$	6.3	**7**, 21
HD 89886	F7V	167.0	$7.44^{0.01}$	$6.09^{0.05}$	$0.273^{0.004}$	1.6	6, **7**
HD 90781	F3V	77.0	$7.448^{0.008}$	$6.51^{0.03}$	$0.198^{0.003}$	1.2	4, **14**, 15
HD 90874	A2V	68.0	$5.991^{0.004}$	$5.86^{0.04}$	$0.237^{0.003}$	0.25	**1**, 2, 3, 4, 8
HD 92945	K1V	21.4	$7.708^{0.007}$	$5.77^{0.05}$	$0.347^{0.005}$	0.21	7, 8
HD 93453	A4IV	72.0	$6.288^{0.004}$	$5.91^{0.03}$	$0.244^{0.003}$	0.4	**1**, 4
HD 105850	A1V	56.1	$5.447^{0.003}$	$5.35^{0.04}$	$0.290^{0.004}$	0.2	**1**, 2, 3, 4, 8, 22
HD 105912	F2/3V	50.0	$6.940^{0.007}$	$5.96^{0.06}$	$0.258^{0.004}$	2.7	1, 2, 3, **8**, 23
HD 106906	F5V	59.0	$7.798^{0.008}$	$6.76^{0.04}$	$0.184^{0.003}$	0.015	1, 2, 3
HD 109573	A0V	67.1	$5.777^{0.004}$	$5.79^{0.04}$	$0.231^{0.003}$	0.01	2, 3, 4, **8**, 22
HD 109704	A3V	68.8	$5.869^{0.003}$	$5.77^{0.05}$	$0.245^{0.003}$	0.4	1, 2, 3, 4, **8**, 22
HD 112603	F2V	61.0	$6.952^{0.004}$	$6.14^{0.05}$	$0.232^{0.003}$	1.5	**1**, 6
HD 117716	A0/1V	72.0	$5.690^{0.004}$	$5.67^{0.03}$	$0.255^{0.003}$	0.3	1, 2, 3, **8**
HD 118972	K1V	15.6	$6.918^{0.004}$	$5.14^{0.05}$	$0.480^{0.006}$	0.3	**1**, 2, 3, 7, 8, 11, 24

Notes. 1σ error bars are given as superscripts. V and H magnitudes are from Kharchenko & Roeser (2009). Limb-darkened stellar diameters ($\theta_{\rm LD}$) are computed from surface-brightness relationships based on the V and K magnitudes, following Kervella et al. (2004). References include previous searches for warm and cold dust around the target stars, with the reference in bold highlighting the origin of the warm dust classification that led to their addition to our sample, where applicable.

References. (1) Patel et al. (2014); (2) Ballering et al. (2013); (3) Cotten & Song (2016) ; (4) David & Hillenbrand (2015); (5) Bonfanti et al. (2016); (6) Holmberg et al. (2009); (7) Vican & Schneider (2014); (8) Chen et al. (2014); (9) Pace (2013); (10) Eiroa et al. (2013); (11) Valenti & Fischer (2005); (12) Delgado Mena et al. (2014); (13) Huensch et al. (1998); (14) Wu et al. (2013); (15) McDonald et al. (2012); (16) Durkan et al. (2016); (17) Tucci Maia et al. (2016); (18) Maldonado et al. (2012); (19) Desidera et al. (2015); (20) Pawellek et al. (2014); (21) Delgado Mena et al. (2015); (22) Mittal et al. (2015); (23) Feltzing et al. (2001); (24) Mamajek & Hillenbrand (2008); (25) De Rosa et al. (2014); (26) Tsantaki et al. (2013); (27) Casagrande et al. (2011); (28) Stark et al. (2014b); (29) Wahhaj et al. (2013); (30) Maire et al. (2014); (31) Zuckerman et al. (2004); (32) Binks & Jeffries (2014); (33) Chauvin et al. (2010).

Table B.1. continued.

Star	Type	Dist. (pc)	V (mag)	H (mag)	θ_{LD} (mas)	Age (Gyr)	References
HD 136544	F6V	74.0	$7.43^{0.01}$	$6.35^{0.03}$	$0.221^{0.004}$	2.0	**1**, 9
HD 141378	A5IV	54.0	$5.522^{0.003}$	$5.27^{0.03}$	$0.306^{0.004}$	0.3	1, 2, **3**, 8, 25
HD 141943	G0/2V	67.0	$7.85^{0.01}$	$6.41^{0.03}$	$0.231^{0.004}$	0.03	3, **8**, 33
HD 142139	A3V	66.0	$5.747^{0.003}$	$5.66^{0.05}$	$0.261^{0.004}$	0.2	**1**, 2, 3, 4, 8
HD 161612	G6/8V	26.9	$7.18^{0.01}$	$5.6^{0.1}$	$0.344^{0.005}$	0.8	**7**, 11, 26
HD 174474	A2V	82.0	$6.169^{0.004}$	$5.89^{0.04}$	$0.236^{0.004}$	0.6	**3**, 4, 14, 15
HD 175073	K1V	24.0	$7.96^{0.01}$	$5.95^{0.03}$	$0.324^{0.005}$	4.1	**1**, 27
HD 178606	F5V	53.0	$6.520^{0.007}$	$5.49^{0.02}$	$0.323^{0.004}$	1.7	**1**, 23
HD 179520	F3V	62.0	$7.092^{0.007}$	$6.24^{0.02}$	$0.232^{0.003}$	0.6	**1**, 3, 23
HD 181327	F5/6V	52.0	$7.035^{0.008}$	$5.98^{0.04}$	$0.263^{0.004}$	0.021	1, 2, 3, 28, 31, 32
HD 184932	F2V	65.0	$8.03^{0.01}$	$6.95^{0.02}$	$0.166^{0.003}$	2.1	**1**, 4
HD 185615	G6IV	43.5	$8.11^{0.01}$	$6.54^{0.03}$	$0.286^{0.004}$	9.2	**7**, 9, 15
HD 191089	F5V	52.0	$7.178^{0.007}$	$6.09^{0.03}$	$0.243^{0.004}$	0.021	1, 3, 8, 22, 31, 32
HD 192758	F0V	62.0	$7.013^{0.008}$	$6.30^{0.04}$	$0.217^{0.004}$	0.04	3, **8**, 29
HD 196141	G3V	37.0	$8.09^{0.01}$	$6.58^{0.03}$	$0.213^{0.004}$	0.4	**7**
HD 205674	F3/5IV	52.0	$7.178^{0.007}$	$6.25^{0.03}$	$0.228^{0.003}$	2.2	**1**, 3, 4, 8
HD 220476	G5V	30.0	$7.611^{0.009}$	$6.11^{0.04}$	$0.276^{0.004}$	0.4	**7**
HD 224228	K3V	22.0	$8.237^{0.009}$	$6.01^{0.03}$	$0.325^{0.005}$	0.1–0.2	**1**, 30

Table B.2. Warm versus cold dust classification for the 68 stars showing the presence of a debris disk in our SED modeling.

Name	W12	W22	M24	IRS	M70	P70	P100	$T_{\rm warm}$ (K)	$T_{\rm cold}$ (K)	$L_{\rm warm}/L_*$ ($\times 10^{-4}$)	$L_{\rm cold}/L_*$ ($\times 10^{-4}$)
*HD 203	O	X	X	X	X	X	X	115	–	1.3	–
HD 2262		O	X	X	X	–	X	122	–	0.095	–
*HD 2834	O	O	X	X	X	–	–	–	96	–	0.12
*HD 3126	O	O	O	O	X	–	–	–	53	–	1.3
HD 7570	O	O	X	X	O	–	X	100	–	0.066	–
*HD 9672	X	X	–	X	X	X	X	153	57	1.6	7.0
*HD 10269	O	X	–	–	–	X	–	120	–	1.3	–
HD 10647	O	O	X	X	X	X	X	100	40	0.62	2.5
*HD 10939	O	X	X	X	X	X	X	190	58	0.15	0.73
HD 11171	O	O	O	–	X	X	X	–	100	–	0.11
*HD 15427	O	X	X	X	X	–	–	101	–	0.33	–
*HD 17848	O	O	X	X	X	X	X	–	61	–	0.42
HD 17925		O		X	X	X	X	–	80	–	0.33
HD 20794 [(a)]		–	O	–	O	O	O	–	80	–	0.022
*HD 23484	O	O	O	O	X	X	X	–	55	–	0.93
*HD 24649	O	X	X	–	–	X	–	–	76	–	1.5
HD 25457		X	X	X	X	–	–	180	60	0.40	0.97
*HD 28287	O	O	–	–	–	X	–	140	–	1.0	–
HD 28355	O	X	X	X	X	–	X	–	88	–	0.41
HD 30495	O	O	O	O	X	X	X	–	59	–	0.32
HD 31295	O	X	X	X	X	–	X	165	61	0.19	0.54
HD 33262		O	O	–	X	–	X	120	–	0.16	–
*HD 36187 [(b)]	O	X	–	–	–	–	–	nc	nc	nc	nc

Notes. Symbols X and O represent respectively a significant excess and the absence of an excess in the considered filter, while a dash denotes a filter where no data (or data of insufficient quality) was available for the considered target. For the IRS data, symbol X is used when the $\pm 1\sigma$ error interval around the measured spectrum is located above the photospheric model for a significant, contiguous part of the wavelength range spanned by the IRS spectrum. The last four columns give the inferred temperature and luminosity of the detected disks ("nc" stands for non-constrained). Asterisks denote the newly observed stars from this study. [(a)]No formal excess detected, but the combination of marginal (close to significant) excesses at 70 and 100 μm is clear evidence for a cold dust population (see also SEDs in Fig. A.1); [(b)]no data available beyond 22 μm, preventing us from determining the temperature and luminosity of the disk; [(c)]temperature constrained to be higher than 100 K by a combination of WISE12, WISE22, and archival IRAS60 & IRAS100 photometry, also giving a rough estimate of disk luminosity (with a large error bar $\sim 10^{-4}$ due to the temperature vs. luminosity degeneracy).

Table B.2. continued.

Name	W12	W22	M24	IRS	M70	P70	P100	$T_{\rm warm}$ (K)	$T_{\rm cold}$ (K)	$L_{\rm warm}/L_*$ ($\times 10^{-4}$)	$L_{\rm cold}/L_*$ ($\times 10^{-4}$)
*HD 37306	O	X	X	X	X	X	X	120	–	0.70	–
*HD 37484	O	X	O	X	X	–	–	150	67	1.4	2.2
HD 38858	O	O	O	X	X	X	–	–	52	–	22
HD 39060	X	X	–	–	X	X	X	290	86	8.1	0.76
HD 40307	O	O	O	X	O	O	O	–	60	–	0.071
HD 45184	O	O	O	X	X	X	–	–	58	–	0.77
*HD 60491	O	O	X	–	X	–	–	–	76	–	2.1
*HD 61005	O	X	X	X	X	X	X	120	53	2.1	24
HD 69830	X	X	X	X	O	–	X	373	–	2.0	–
HD 71155	X	X	X	–	X	X	X	109	–	0.28	–
*HD 71722	O	X	X	X	X	–	X	210	73	0.28	0.76
*HD 76143 [c]	O	X	–	–	–	–	–	>100	–	∼2	–
HD 76151	O	O	O	X	X	–	X	103	–	0.14	–
*HD 89886 [b]	O	X	–	–	–	–		nc	nc	nc	nc
*HD 90874	O	O	O	X	O	–	–	148	–	0.12	–
HD 91324		O	O	X	O	–	–	–	80	–	0.053
*HD 92945	O	O	O	O	X	X	–	–	34	–	6.8
*HD 105850	X	X	X	X	O	–	–	161	–	0.28	–
*HD 105912	O	X	X	X	X	–	–	111	–	0.84	–
*HD 109573	X	X	–	X	O	X	X	–	97	–	44
HD 109704	O	X	X	X	O	–	–	140	–	0.40	–
HD 115617	O	X	O	X	X	X	X	–	59	–	0.23
*HD 117716	X	O	X	X	O	–	–	150	–	0.085	–
*HD 118972	O	O	O	X	X	–	X	–	95	–	0.41
HD 135379		X	X	X	O	–	–	173	–	0.44	–
HD 139664	O	O	–	–	X	X	–	–	74	–	1.26
*HD 141943	O	X	X	X	O	–	–	102	–	0.83	–
HD 160032		O	O	X	O	–	X	–	78	–	0.053
HD 172555	X	X	X	X	X	X	X	190	–	5.14	–
*HD 174474	O	X	–	–	–	X	–	280	–	0.92	–
HD 178253	O	X	X	X	X	–	–	164	–	0.17	–
*HD 179520	O	X	–	–	–	X	–	160	–	1.48	–
*HD 181327	O	X	X	X	X	–	X	–	80	–	27
HD 188228	O	O	O	X	X	X	X	–	80	–	0.041
*HD 191089	O	X	X	–	X	–	X	–	94	–	15
HD 192425	O	X	X	X	X	–	X	210	57	0.26	0.36
*HD 192758	O	X	X	X	X	–	X	–	64	–	5.0
HD 195627	O	O	X	X	X	X	X	140	45	0.15	0.90
*HD 205674	O	O	X	X	X	–	X	–	55	–	3.4
HD 206860	O	O	O	X	O	–	X	–	85	–	0.082
HD 207129	O	O	O	X	X	X	X	–	45	–	0.91
HD 213845 [a]	O	O	O	O	O	–	O	–	80	–	0.032
HD 216435	O	O	–	O	X	X	–	–	50	–	0.18
HD 219482	O	O	X	X	X	X	X	–	86	–	0.27
*HD 224228	O	O	X	–	O	–	–	130	–	0.61	–

Table B.3. Sublimation radius, sensitivity reduction factor (ϕ), and effective sensitivity ($\sigma_{\rm eff}$) for the combined sample of 133 stars, computed for a sublimation temperature of 1500 K under blackbody assumption.

Name	Subl. rad. (au)	Subl. rad. (mas)	ϕ	$\sigma_{\rm eff}$ (%)
HD 142	0.06	2.29	0.25	1.06
*HD 203	0.08	1.94	0.90	0.25
HD 1581	0.04	4.60	0.70	0.44
HD 2262	0.12	5.02	0.77	0.23
*HD 2834	0.22	4.18	1.16	0.73
*HD 3126	0.06	1.43	0.59	0.40
HD 3302	0.09	2.52	0.29	0.89
HD 3823	0.05	2.20	0.23	0.97
*HD 4113	0.04	0.90	0.29	0.69
HD 7570	0.05	3.15	0.42	0.62
HD 7788	0.07	3.42	0.48	0.36
*HD 9672	0.17	2.82	1.23	0.26
*HD 10269	0.06	1.27	0.49	0.28
HD 10647	0.04	2.36	0.26	1.01
*HD 10939	0.22	3.49	1.26	0.26
HD 11171	0.06	2.43	0.27	1.55
HD 14412	0.02	1.83	0.16	1.30
HD 15008	0.21	5.00	0.77	0.42
*HD 15427	0.14	2.95	1.25	0.14
HD 17051	0.05	2.72	0.33	0.70
*HD 17848	0.16	3.24	1.26	0.11
HD 17925	0.02	2.23	0.23	0.99
HD 19107	0.11	2.75	0.34	0.63
HD 20766	0.03	2.49	0.28	0.92
HD 20794	0.03	4.36	0.66	0.56
HD 20807	0.03	2.89	0.36	1.46
HD 22001	0.08	3.64	0.52	0.39
*HD 23484	0.02	1.27	0.49	0.52
*HD 24649	0.05	1.26	0.49	0.46
HD 25457	0.05	2.65	0.31	0.45
*HD 28287	0.02	0.64	0.16	1.97
HD 28355	0.15	3.08	0.40	0.22
*HD 29137	0.05	0.91	0.30	0.53
HD 30495	0.03	2.62	0.31	0.67
HD 31295	0.14	4.05	0.60	0.25
HD 31925	0.10	2.48	0.28	0.79
HD 33111	0.24	8.62	0.96	0.43
HD 33262	0.04	3.79	0.55	0.38
HD 34721	0.05	2.03	0.20	1.06
*HD 36187	0.25	2.89	1.24	0.11
*HD 37306	0.13	1.99	0.92	0.16
*HD 37484	0.07	1.18	0.44	0.47
HD 38858	0.03	2.16	0.22	1.31
*HD 38949	0.04	0.85	0.26	0.68
HD 39060	0.11	5.66	0.82	0.28
HD 40307	0.02	1.48	0.11	2.18
*HD 41278	0.06	1.11	0.40	0.54
HD 43162	0.03	1.76	0.15	1.40
*HD 44524	0.11	1.05	0.37	0.54
HD 45184	0.04	1.75	0.15	1.00
HD 53705	0.04	2.17	0.22	1.04
HD 56537	0.21	6.72	0.90	0.28
*HD 60491	0.02	0.79	0.23	0.69
*HD 61005	0.03	0.83	0.25	0.48
HD 69830	0.03	2.20	0.23	1.15
HD 71155	0.22	5.90	0.84	0.30
*HD 71722	0.18	2.46	1.13	0.15
HD 72673	0.02	1.88	0.17	1.90
*HD 76143	0.14	2.70	1.20	0.15
HD 76151	0.04	2.04	0.20	1.42
HD 76932	0.05	2.19	0.23	1.85
*HD 80883	0.05	0.73	0.20	0.88
HD 82434	0.11	5.73	0.83	0.70
HD 88955	0.17	5.46	0.80	0.31
*HD 89886	0.18	1.10	0.39	0.68
HD 90132	0.11	2.67	0.32	1.28
HD 90781	0.08	1.08	0.38	0.42
*HD 90874	0.15	2.19	1.01	0.13
HD 91324	0.07	3.36	0.46	0.37
*HD 92945	0.02	0.91	0.30	0.60
HD 99211	0.12	4.67	0.71	0.31
HD 102365	0.03	3.34	0.46	0.50
HD 104731	0.07	2.81	0.35	0.40
*HD 105850	0.17	2.99	1.25	0.14
*HD 105912	0.06	1.28	0.50	0.30
HD 108767	0.26	9.72	0.96	0.16
*HD 109573	0.17	2.53	1.15	0.13
HD 109704	0.14	2.07	0.96	0.13
HD 109787	0.20	5.05	0.77	0.26
*HD 112603	0.08	1.30	0.52	0.49
HD 115617	0.03	4.04	0.60	0.38
*HD 117716	0.19	2.63	1.18	0.15
*HD 118972	0.02	1.26	0.49	0.19
HD 120136	0.06	4.06	0.60	0.37
HD 128898	0.10	6.32	0.87	0.25
HD 129502	0.09	5.17	0.78	0.18
HD 130109	0.27	6.56	0.89	0.48
HD 134083	0.06	3.25	0.44	1.07
HD 135379	0.15	4.92	0.75	0.49
HD 136202	0.07	2.67	0.32	2.00
*HD 136544	0.08	1.07	0.38	0.93
HD 139664	0.06	3.68	0.52	0.36
HD 141891	0.10	8.43	0.96	0.21
*HD 141943	0.05	0.90	0.29	0.69
HD 149661	0.02	2.44	0.27	0.81
HD 152391	0.03	1.66	0.13	1.34
HD 160032	0.07	3.27	0.44	0.25
HD 160915	0.05	2.89	0.36	0.77
*HD 161612	0.03	1.10	0.40	0.30
HD 164259	0.09	3.68	0.52	0.36
HD 165777	0.15	5.58	0.81	0.34
HD 172555	0.10	3.44	0.48	0.53
*HD 174474	0.18	2.18	1.01	0.19
HD 178253	0.18	4.67	0.71	0.50
*HD 179520	0.08	1.26	0.49	0.50
*HD 181327	0.07	1.27	0.49	0.32
HD 182572	0.05	3.06	0.40	0.33
*HD 185615	0.03	0.80	0.23	1.37
HD 188228	0.23	7.27	0.94	0.29
*HD 191089	0.06	1.23	0.46	1.04

Notes. Asterisks denote the newly observed stars on the medium-sized AT configuration, while the other stars were observed on the compact AT configuration by Ertel et al. (2014).

Table B.3. continued.

Name	Subl. rad. (au)	Subl. rad. (mas)	ϕ	$\sigma_{\rm eff}$ (%)
HD 192425	0.16	3.49	0.49	0.51
*HD 192758	0.08	1.24	0.48	0.60
HD 195627	0.10	3.43	0.48	1.09
*HD 196141	0.03	0.79	0.23	0.86
HD 197157	0.10	4.04	0.60	0.50
HD 197692	0.07	4.72	0.72	0.28
HD 203608	0.04	4.47	0.68	0.50
*HD 205674	0.06	1.20	0.45	1.11
HD 206860	0.04	2.06	0.20	1.48
HD 207129	0.04	2.51	0.28	0.63
HD 210049	0.17	4.15	0.62	0.61
HD 210277	0.04	1.71	0.14	2.14
HD 210302	0.06	3.24	0.44	0.57
HD 210418	0.18	6.35	0.87	0.33
HD 213845	0.06	2.56	0.30	0.80
HD 214953	0.05	2.18	0.22	1.00
HD 215648	0.07	4.59	0.70	0.31
HD 215789	0.30	7.63	0.96	0.27
HD 216435	0.06	1.89	0.17	1.56
HD 219482	0.05	2.40	0.26	0.64
HD 219571	0.11	4.89	0.75	0.36
*HD 220476	0.03	0.97	0.33	0.54
*HD 224228	0.02	0.82	0.24	1.64